Natural Hazards
and Earth System
Sciences

Characterizing the scale of regional landslide triggering from storm hydrometeorology

Jonathan Perkins[1], **Nina S. Oakley**[2,3], **Brian D. Collins**[1], **Skye C. Corbett**[1], and **W. Paul Burgess**[4]

[1]US Geological Survey, Geology, Minerals, Energy, and Geophysics Science Center, Moffett Field, CA 94035, USA
[2]Center for Western Weather and Water Extremes, Scripps Institution of Oceanography, San Diego, CA 92037, USA
[3]California Geological Survey, Santa Rosa, CA 95405, USA
[4]California Geological Survey, Los Angeles, CA 90013, USA

Correspondence: Jonathan Perkins (jperkins@usgs.gov)

Abstract. Rainfall strongly affects landslide triggering; however, understanding how storm characteristics relate to the severity of landslides at the regional scale has thus far remained unclear, despite the societal benefits that would result from defining this relationship. As mapped landslide inventories typically cover a small region relative to a storm system, here we develop a dimensionless index for landslide-inducing rainfall, A^*, based on extremes of modeled soil water relative to its local climatology. We calibrate A^* using four landslide inventories, comprising over 11 000 individual landslides over four unique storm events, and find that a common threshold can be applied to estimate regional shallow-landslide-triggering potential across diverse climatic regimes in California (USA). We then use the spatial distribution of A^*, along with topography, to calculate the landslide potential area (LPA) for nine landslide-inducing storm events over the past 20 years, and we test whether atmospheric metrics describing the strength of landfalling storms, such as integrated water vapor transport, correlate with the magnitude of hazardous landslide-inducing rainfall. We find that although the events with the largest LPA do occur during exceptional atmospheric river (AR) storms, the strength of landfalling atmospheric rivers does not scale neatly with landslide potential area, and even exceptionally strong ARs may yield minimal landslide impacts. Other factors, such as antecedent soil moisture driven by storm frequency and mesoscale precipitation features within storms, are instead more likely to dictate the patterns of landslide-generating rainfall throughout the state.

1 Introduction

Rainfall-induced landslides are a global hazard that result in thousands of fatalities (Petley, 2012; Froude and Petley, 2018) and billions of dollars in economic losses annually (Schuster and Fleming, 1986; Kjekstad and Highland, 2009). During the progression of a hazardous storm, shallow landslides, those occurring primarily within a soil-mantled hillslope, are often triggered by infiltrating rainwater that interacts with the shallow (typically less than 3 m) groundwater system to produce destabilizing pore water pressures (Reid, 1994; Iverson, 2000; Collins and Znidarcic, 2004; Bogaard and Greco, 2016) (Fig. 1). Over the past 5 decades, a growing recognition of rainfall-induced landslide hazards has led to a range of efforts in developing landslide warning systems that assess when these rainfall thresholds for slope failure might be exceeded using a variety of criteria (Campbell, 1975; Keefer et al., 1987; Baum and Godt, 2010; Kirschbaum and Stanley, 2018; Guzzetti et al., 2020, and references therein).

While operational forecasting of landslides using numerical weather prediction remains rare (e.g., Guzzetti et al., 2020; Kong et al., 2020), a growing body of research suggests that distinct meteorological features at both the synoptic scale ($\sim$ 200 to 2000 km, multiple days) and the mesoscale ($\sim$ 2–200 km, minutes to hours) can exert a strong control on landslide occurrence and distribution and could potentially be used for landslide forecasting. For example, atmospheric rivers (ARs) are synoptic features consisting of long filaments of enhanced water vapor in the lower atmosphere and are typically associated with mid-latitude cy-
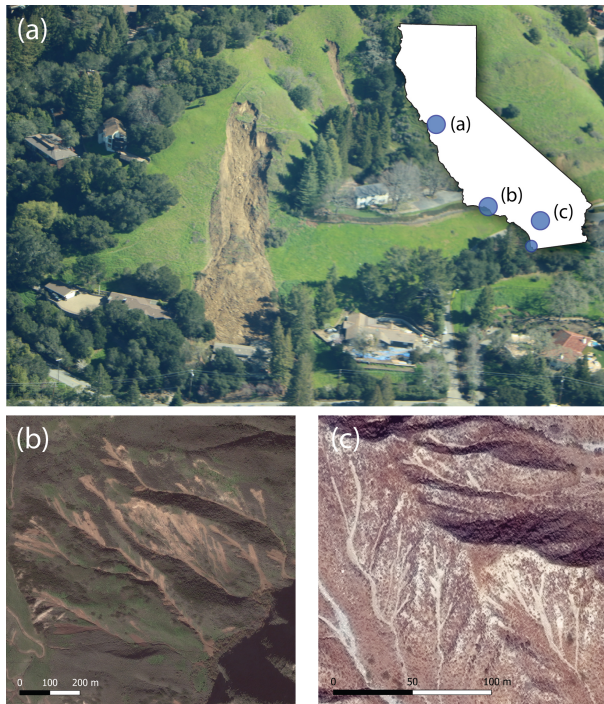
Figure 1. Examples of landslides triggered by recent storms in California. **(a)** Aerial photograph of a home in California's East Bay region damaged by a landslide initiated during an atmospheric river storm on 6 February 2017. Photo taken by Brian Collins. **(b)** WorldView-2 imagery of landslides triggered by heavy rainfall on 10 January 2005, near the town of La Conchita. **(c)** WorldView-3 imagery of the southernmost San Bernardino Mountains north of Cabazon, showing debris flows triggered by the 14 February 2019 atmospheric river storm that caused extensive damage across Riverside County. Inset shows a map of California with the annotated circles corresponding to the respective panel. The unlabeled small blue circle corresponds to the location of the landslide inventory associated with a storm in April 2020 that triggered numerous landslides near the town of Encinitas (Fig. 3d).

clones that transport moisture poleward from the tropics to the mid-latitudes, such as the west coast of the United States. They are a primary generator of precipitation in California (USA) and are typically measured and denoted by integrated water vapor transport (IVT) values exceeding $250 \, \mathrm{kg \, m^{-1} \, s^{-1}}$ (Ralph et al., 2019). Combining news reports of landslide events going back nearly 150 years with an AR catalogue, Cordeira et al. (2019) showed that in California's San Francisco Bay Area, 70 %–80 % of reported landslide days occur in association with AR conditions. However, the authors also found that only 5 %–12 % of ARs in their catalogue coincided with reported landslide days, leading them to suggest that other meteorological processes may have accompanied these storms to trigger the reported landslides. Similarly, Oakley et al. (2018) found that 60 %–90 % of rainfall events exceeding published landslide-triggering thresholds in California over a 22-year period coincided

with storms featuring ARs. At a smaller dynamic scale, mesoscale processes that operate within synoptic storms and that are shorter-lived phenomena compared to ARs can provide bursts of higher-intensity rainfall that can also trigger abundant landsliding. Collins et al. (2020) found a close spatial clustering between distributed shallow landslides from a 2018 storm in central California and the stalling of a narrow cold-frontal rainband (NCFR; a band of intense convective rainfall that can occur ahead of a cold front) that followed the passage of an atmospheric river over the region. Here, the timing of landslide triggering coincided with the NCFR rather than the AR, though rainfall associated with the AR likely primed susceptible slopes for later triggering (Collins et al., 2020). Thus, storm characteristics at both the synoptic scale and the mesoscale can play an important role in shallow-landslide occurrence and distribution, and efforts to forecast landslide occurrence could benefit from assessing the likelihood of these meteorological processes occurring over particular landscapes.

Evaluating the magnitude of landslide hazard potential across the footprint of a given storm event requires some way to estimate landslide triggering. Rainfall intensity–duration thresholds are a common empirical method used to assess the landslide potential for a given storm event (Cannon and Ellen, 1985; Keefer et al., 1987; Larsen and Simon, 1993; Guzzetti et al., 2008). These relationships are typically calibrated regionally (or at a specific site near a rain gauge) and generally follow a power-law relationship where the triggering rainfall intensity declines exponentially with storm duration. This exponential relationship between rainfall intensity and duration for landslide triggering implies that higher-intensity storms require less rainfall depth to trigger landslides than lower-intensity storms, which is known to be related to the nonlinear soil moisture storage characteristics that dictate the transmission rate of infiltrating pore water (Green and Ampt, 1911; Richardson, 1922; Richards, 1931; Lu et al., 2011). In landscapes that do not rapidly drain between storm events, antecedent rainfall may lower the amount of rainfall needed to reach critically unstable pore water pressure (Crozier and Eyles, 1980; Crozier, 1999; Glade et al., 2000; Bogaard and Greco, 2018).

Incorporating antecedent moisture into regional estimates of slope stability has taken several forms. Thomas et al. (2018) considered antecedent soil moisture and rainfall depth thresholds for driving positive pore water pressure in soil columns using physically based infiltration models (i.e., using the Richards equation; Richards, 1931). They found a nonlinear relationship between antecedent soil moisture and the necessary rainfall depth to generate pore water pressures that trigger shallow-landslide initiation in California's San Francisco Bay region. The nonlinearity results from the shape of the soil water characteristic curves: as soil saturates from dry to wet conditions, the soil hydraulic conductivity increases by several orders of magnitude (e.g., van Genuchten, 1980), resulting in increasingly fast transmission of pore wa-

ter from the surface to the water table. The antecedent water index (AWI) proposed by Godt et al. (2006) uses only rainfall data in a one-dimensional mass balance model initially derived by Wilson and Wieczorek (1995) that tracks theoretical predictions of soil water throughout a rainy season. This class of reduced-complexity soil hydrologic models is commonly referred to as "leaky-barrel" or "tank" models, where rainfall immediately enters the model reservoir and drains at a rate proportional to the reservoir height. While AWI does not directly incorporate the physical processes of rainfall infiltration into the soil surface (i.e., it does not use the nonlinear soil water characteristic curve relationships upon which the Richards equation is based), the model has nevertheless proven to capture the dynamics of a range of soil hydrologic processes. While Wilson and Wieczorek (1995) calibrated their model to observed changes in pore water pressure for a landslide early warning system in the San Francisco Bay Area, Godt et al. (2006) calibrated AWI to local measurements of soil water content and used an AWI threshold as part of a decision tree to forecast landslide events in the Seattle, Washington (USA), region. Similarly, the Japanese Meteorological Agency used a three-tank model calibrated to a specific watershed to develop a soil water index (SWI) that has been used to help establish rainfall-induced landslide thresholds across the country (Okada et al., 2001; Saito and Matsuyama, 2012). Additional examples of hydrometeorological thresholds used in various landslide forecasting frameworks can be found in Mirus et al. (2024).

Regional variability also plays a role in setting rainfall thresholds, and several studies have used various forms of normalization of rainfall and/or soil moisture variables to account for this variability (Cannon and Ellen, 1985; Keefer, 1987; Wilson, 1997; Guzzetti et al., 2008; Saito et al., 2010; Peruccacci et al., 2017). Cannon (1988) normalized rainfall totals by the gauge-specific mean annual precipitation (MAP) to account for regional differences in triggering rainfall. Wilson and Jayko (1997) later updated Cannon's maps using the "rainy day normal" (where RDN is MAP divided by the number of rainy days) to further account for regional differences in triggering. They noted that the recurrence interval of storm events is important in the equilibrium of landscapes. Marc et al. (2019) tested the efficacy of the 10-year recurrence 48 h rainfall anomaly (R_{48}^*) as a predictor of shallow-landslide concentration in Japan and showed that a strong correlation exists between landslide concentration and the magnitude of the rainfall anomaly. For the same storm, Saito and Matsuyama (2012) showed that normalizing the SWI by its locally maximum value over the preceding decade also correlated with a clustering of landslides.

Wilson and Jayko (1997), Peruccacci et al. (2017), and Marc et al. (2019) all posited that landscapes may experience some degree of geomorphic tuning to extreme rainfall, and there are several potential reasons why either climatology or locally extreme rain might shape landscapes in ways that result in varying landslide-triggering thresholds

across climates. For example, soil production and hence soil thickness can change with increasing mean annual precipitation (Richardson et al., 2019; Pelletier et al., 2016). This may have either a destabilizing effect through increasing soil thickness or a stabilizing effect by lowering hillslope gradients through enhanced diffusivity. Furthermore, root reinforcement of hillslopes is controlled by vegetation density (e.g., Schmidt et al., 2001), which also varies with precipitation (Nemani et al., 2002; Tao et al., 2016). Additionally, theoretical and numerical work shows that local rainfall intensity can alter long-term landscapes by changing factors like drainage density and mean slope (Tucker and Slingerland, 1997), which in turn can lead to nonlinear increases in runoff (Carlston, 1963) that can subsequently drive shallow-landslide and debris flow initiation. Thus, there is a strong conceptual basis for the normalization of rainfall thresholds with respect to the regional climatology of their respective landscapes.

Quantifying the overall strength of storms that trigger shallow landslides also remains an ongoing challenge. One way to characterize distributed storm strength is with the R-CAT scale (Ralph and Dettinger, 2012; Lamjiri et al., 2020), which uses 3 d precipitation totals from distributed rain gauges to delineate broad categories of storm strength, from R-CAT 1 to R-CAT 4. This allows for intercomparison of extreme-rainfall events over the past century when sufficient gauge data exist. On a broader scale, the atmospheric river (AR) scale (Ralph et al., 2019) uses the magnitude and duration of the vertically integrated water vapor transport (IVT) to categorize the relative strength of atmospheric rivers on a scale of AR1 to AR5 at a point. Although not a direct measurement of rainfall, this characterization avoids the dependence of storm impact prediction on site-specific rain gauge data. AR-scale values are suggested to correspond to a balance between beneficial and hazardous conditions, with an AR1 event representing primarily beneficial rainfall and an AR5 event representing primarily hazardous rainfall, yet the authors stress that these are only general guidelines and may often not be the case (Ralph et al., 2019). Although the R-CAT and AR scales allow for intercomparison of storm rainfall or IVT characteristics, they do not specifically represent landslide hazard. For example, if an R-CAT 4 or an AR5 event occurs when soil conditions are dry, they might produce fewer (or no) landslides than if elevated soil moisture conditions were present preceding the storm event. These considerations warrant a more hazard-focused characterization of storms.

A primary aim of this study is to develop a simple hydrometeorological metric that can be used to delineate conditions consistent with regional shallow-landslide occurrence and that can be mapped in space and time. Combining aspects of the rainfall anomaly approaches of both Marc et al. (2019) and Saito and Matsuyama (2012), here we develop a universal index for landslide triggering based on an anomalous values of theoretical soil water derived from the hydrologic tank model of Godt et al. (2006) and Wilson and Wieczorek

(1995), which we call A^* (Eq. 1). To test the methodology, we use landslide inventories from four storms that span both arid and temperate regions of California, a vast and notably geomorphically and climatically diverse region. We show that in the case of our four study inventories, a threshold of A^* can be utilized to identify landslide events in both space and time, which bolsters the use of A^* to broadly estimate regionally hazardous rainfall conditions outside the areas of mapped landslides.

To estimate the footprint of potentially hazardous (i.e., shallow-landslide-inducing) rainfall across the state, we measure the distribution of hillslopes impacted by above-threshold A^* for each storm to define a landslide potential area (LPA). A similar approach has been used effectively in studies quantifying the impacts of earthquake-induced landslides by considering both ground shaking and topographic metrics. For example, Marc et al. (2017) utilize seismic scaling relationships and topographic slope to delineate a cumulative landslide-affected area resulting from an earthquake, and Tanyas and Lombardo (2019) consider the role of both peak ground acceleration and topographic slope and relief to map coseismic landslide-affected areas.

We then investigate how the magnitude and spatial pattern of landslide-inducing conditions relate to meteorological process strength and spatial extent. We apply our methodology to a diverse set of nine impactful landslide-inducing storms across California from 2005–2021 (including the four calibration events). California's landscape encompasses 11 mapped geomorphic provinces distinct in their climatic and topographic characteristics (Jenkins, 1938) and therefore provides an ideal study area in which to evaluate the utility of our hazard index, A^*, which represents theoretical estimates of anomalous soil water against highly variable climatological conditions. To examine how the strength of AR conditions relates to the severity of shallow landsliding, we compare the landslide potential area (LPA) with the AR scale (Ralph et al., 2019) and show that, while ARs are clearly important drivers of the events in our catalogue, antecedent conditions, controlled by factors such as AR frequency, and mesoscale features, which often define the distribution of brief but intense periods of rainfall, rather than individual AR strength appear to exert a dominant control on shallow landsliding and should therefore be assessed when examining patterns of landslide-inducing rainfall.

2 Methods

2.1 Development of dimensionless landslide index A^*

Here we develop a proxy for rainfall-induced shallow-landslide potential by establishing a normalized index, A^*, which represents extreme values of the antecedent water index (AWI) relative to its local climatology:

$$A^* = \frac{\text{AWI}}{\text{AWI}_{\text{RI}}}, \tag{1}$$

where AWI_{RI} is the value of AWI at a given recurrence interval (RI). This is similar to the normalized rainfall metric R^* proposed by Marc et al. (2019) and also conceptually similar to the normalized soil water index pioneered by Okada et al. (2001) and Saito and Matsuyama (2012); however, here we use the hydrologic tank framework of AWI since it does not rely on a specifically calibrated and more complex three-tank model and has already been effectively utilized in applications of landslide forecasting along the United States west coast (Wilson and Wieczorek, 1995; Godt et al., 2006). Similar leaky-bucket models have also been utilized to explore controls on monsoonal landslides in the Himalayas (Gabet et al., 2004; Burrows et al., 2023).

Importantly, this approach using A^* to define a universal hydrometeorological landslide hazard index does not explicitly assess the susceptibility of individual slopes to rainfall-induced failure as is commonly done for physically based models of shallow slope stability (e.g., Montgomery and Dietrich, 1994; Baum et al., 2008). Rather, the normalization process is purposefully focused on a broader, regional scale. At this coarse spatial scale, we argue that distributions of A^* illustrate overall patterns of hazardous rainfall and therefore help provide a framework for intercomparison of storms and the meteorological conditions associated with rainfall-induced landslides.

The AWI used in our study was formalized by Godt et al. (2006) to develop a landslide forecast system for Seattle, Washington (USA). The index provides a measure of theoretical soil water using a simple hydrologic tank model developed by Wilson and Wieczorek (1995). The tank model employs a mass balance where rainfall is immediately added to a reservoir with a lower outlet that drains proportionally to the water level in the reservoir. In the model design, reservoir drainage does not occur until sufficient rain has fallen to completely fill soil pores bound by capillarity that restrict water flow. This filling parameter is termed R_0 and herein taken to be equal to 0.180 m (Godt et al., 2006), which is approximately the amount of water needed to bring 1 m thick loamy soil to field capacity. Once the seasonal rainfall depth exceeds R_0, the flux of additional soil water not bound by capillarity is modeled as follows:

$$\text{AWI}_t = \text{AWI}_{t-1} e^{-k_{\text{d}} \Delta t} + \frac{I_i}{k_{\text{d}}} (1 - e^{-k_{\text{d}} \Delta t}), \tag{2}$$

where I_i is the rainfall rate added to the reservoir $[\text{m h}^{-1}]$, k_{d} is a drainage constant that modulates the flux out of the system $[\text{h}^{-1}]$, Δt is the time step $[\text{h}]$, and the first term in the equation is the value of AWI $[\text{m}]$ at the previous time step $(t-1)$ that has experienced drainage over Δt. Following rainfall, AWI decays back toward zero. The model assumes that Δt exceeds the timescale required for infiltrating

rainwater to integrate fully with the existing pore water in the soil. The model also resets at the beginning of each water year to its initial condition ($-R_0$), which approximates the impact of processes like evapotranspiration that tend to dry soils from their field capacity back toward their residual moisture content. Application of this methodology to regions outside of Mediterranean climates, like those within our study area, may require further testing or a more direct incorporation of evapotranspiration processes. While the constant k_d in Eq. (2) may influence the local magnitude of AWI, for A^* only the relative value is important for a given grid cell. For the case of the soil water index, the changing rate constant does not significantly impact the relative distribution of peaks (Osanai et al., 2010), and we conduct a similar sensitivity analysis here. Lastly, although this model does not directly consider the physical processes of infiltration through the vadose zone into a shallow unconfined aquifer (e.g., Iverson, 2000; Collins and Znidarcic, 2004; Thomas et al., 2018), given that we are modeling changes in seasonal average moisture storage, the model simplifications are reasonable for a depth-averaged estimate of soil moisture, and Wilson and Wieczorek (1995) and Godt et al. (2006) both show that the model can replicate changes in pore water pressure and soil moisture that have been used as part of landslide early warning systems in both northern California and Seattle, Washington, respectively. Here we regard AWI as reflecting a general mass balance of soil water, and we do not attempt to tie AWI to a specific measurable soil variable such as moisture content or pore pressure.

Estimating the spatial distribution of AWI$_{RI}$ (the recurrence value estimates of AWI) across our study area required calculating an AWI climatology using a gridded precipitation dataset from which we could estimate local AWI values at varying recurrence intervals. Here we used 4 km grids of 6-hourly rainfall from the National Oceanic and Atmospheric Administration (NOAA) California Nevada River Forecast Center (CNRFC) Stage IV quantitative precipitation estimate (QPE) (Seo and Breidenbach, 2002; Nelson et al., 2016; CNRFC, 2023a). These precipitation products are generated by interpolating rain gauge data using the elevation–precipitation relationships established by the PRISM Climate Group (PRISM, 2014). Unlike other NOAA river forecast centers, because of poor radar coverage in crucial mountainous areas in California, the CNRFC does not incorporate radar data in their QPE (Nelson et al., 2016). From this archive of gridded precipitation estimates we calculated 6-hourly AWI for water years 2004–2022 across the state of California. To then calculate AWI$_{RI}$ values for each grid cell, we used a block maxima method (i.e., taking each annual maximum of AWI for each water year) to create generalized extreme value distributions from which we calculated local recurrence intervals along each grid cell (e.g., Marc et al., 2019). Figure 2 illustrates the methodology for an example pixel in our study domain. Panel (a) shows the 19-year time series of rainfall for a representative pixel in southern California, and panel (b) shows the AWI model results calculated from the rainfall data, with annual maxima shown as open circles. These annual maxima are then plotted as a histogram (panel c) from which an extreme value distribution can be fit (blue line). Recurrence intervals can then be directly estimated from the best-fit distribution. As is discussed in Sect. 4.1, for this analysis we selected the 10-year recurrence interval for AWI$_{RI}$, and the resulting grid was smoothed with a median filter to ensure continuity between pixels.

2.2 Determination of a common A^* threshold using four rainfall-induced landslide inventories in California

We determine a common A^* threshold using a series of four landslide-inducing storms that impacted different regions of California from 2005–2020 (Fig. 3). These events were chosen either because landslide inventories already existed or because they could easily be mapped from available satellite data. The four calibration events include a January 2005 storm that produced abundant landsliding throughout southern California (Corbett and Perkins, 2024a; Table 1), including the tragic La Conchita landslide that claimed 10 lives during the event (Jibson, 2006); a January 2017 storm that produced thousands of landslides in the East Bay hills of the San Francisco Bay Area (Corbett and Collins, 2023; Thomas et al., 2018); a February 2019 storm that produced landslides both in the northern San Francisco Bay Area and in southern California's Riverside County (Hatchett et al., 2020; Corbett and Perkins, 2024b); and an April 2020 storm that produced localized landslides and debris flows north of San Diego (Oakley et al., 2020; Reported California Landslides Database, 2025) (Table 1). These inventories together yield a total of 11 668 individual landslides.

To find a threshold that is consistent with all four storms, we first compare the maximum AWI for each landslide point (i.e., 11 688 points) during the passage of each storm against its background AWI value (as discussed below, we use the 10-year recurrence value). This serves as a simple test to see whether the triggering AWI is a constant threshold across different regions in California, which would plot as a horizontal line, or whether any threshold depends on the background AWI itself (see Cavagnaro et al., 2023). As the landslide spacing is small relative to the 4 km grid cells of the AWI dataset, we use the grdtrack function within the PyGMT software package (Tian et al., 2025) that interpolates a precise value between neighboring grid cells. After identifying an acceptable common AWI recurrence interval for normalizing A^* (see Results), we also examined the 19-year time series of A^* across each inventory to illustrate the unique occurrence of these values throughout each of the four calibration storms.
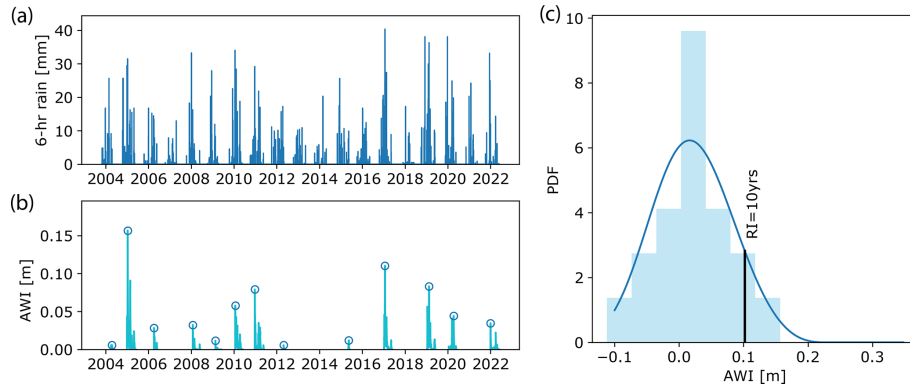
Figure 2. An example from southern California showing the methodology for calculating a climatology of AWI (**b**) using a 19-year record of 6-hourly rainfall (**a**). AWI annual maxima are shown as open circles in (**b**), and years whose maxima are below zero (indicating that antecedent conditions were not met in this water year) are not shown. A generalized extreme value distribution is fit to a histogram of AWI annual maxima (**c**) from which any recurrence interval can be calculated. Here the 10-year recurrence value is shown as the bold black line in (**c**).
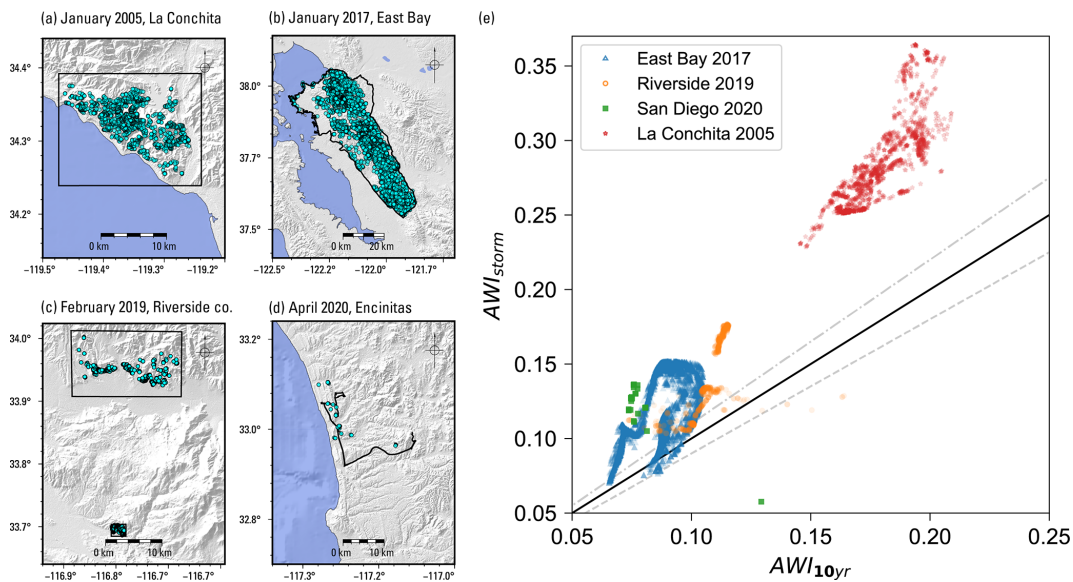
Figure 3. Landslide inventories (**a–d**) used to estimate a reasonable antecedent water index (AWI) recurrence threshold above which most landslides occurred. The black boxes and polygon in panels (**a–c**) represent the landslide mapping bounds for each event, and the black line in panel (**d**) represents the GPS tracks from the California Geological Survey (CGS) field mapping campaign. Panel (**e**) shows a plot of peak AWI modeled during the storm windows interpolated into each landslide point (y axis) against the 10-year recurrence AWI at each point (x axis). A constant threshold across regions would plot as a horizontal line. Over 97 % of the mapped landslides plot above their 10-year recurrence value (the 1 : 1 line). Dashed lines are the 0.9 : 1 and 1.1 : 1 lines. Shaded relief for (**a–d**) is derived from NASA's SRTM 30 m digital elevation model (DEM) (NASA, 2013).

2.3 Calculating the footprint of hazardous rainfall using landslide potential area (LPA)

One of the main goals of our study was to develop a methodology for both dynamically mapping conditions across the state in a way that is consistent with distributed shallow landsliding and for estimating the magnitude of the potential landslide-affected area associated with a given storm. Our approach was to use A^* as an index for distributed shallow-

landslide occurrence and then calculate the spatial distributions of maximum A^* throughout the passage of a storm (Table 1). To do this, we identified the time window bracketing the passage of each storm over land (typically of the order of 72 h; Table 1) and then calculated the maximum of A^* for each pixel in the domain. The landslide potential area (LPA) is then calculated simply as the area of hillslopes in our study area (units of km^2) with $A^* > 1$. To exclude flat terrain (i.e., not capable of shallow landsliding) and terrain

Table 1. Event catalogue of storms used in the analysis. The synoptic features column indicates whether the event featured a closed or cutoff low-pressure system or an atmospheric river (AR), two synoptic-scale features commonly associated with impactful rainfall events in California (CA). The mesoscale features column indicates whether a mesoscale feature producing high-intensity rainfall (i.e., reflectivity > 45 dBZ) was observed in radar imagery in the area where landslides were observed at the approximate time of landslide occurrence. Embedded convection refers to localized areas of high-intensity rainfall embedded within the broader storm system. En dashes indicate no observed features. Also indicated for each event are the measured atmospheric river (AR) scale using the methodology of Ralph et al. (2019) and the calculated landslide potential area (LPA).

Event name and primary impacted regions in CA	Start date	End date	Synoptic features	Mesoscale features	AR scale	LPA (km^2)
January 2005. Transverse Ranges	7 Jan 2005	11 Jan 2005	AR, closed low	Embedded convection	3	11 950
February 2005. Southern CA, Chino Hills	18 Feb 2005	21 Feb 2005	Cutoff low	Embedded convection	1	6160
December 2005. Northern CA, Coast Ranges, Klamath, Sierra Nevada	26 Dec 2005	3 Jan 2006	AR	Ring-like band of moderate rainfall	4	38 600
January 2017. Northern CA	8 Jan 2017	10 Jan 2017	AR	Convective bands in the Sierra Nevada, San Francisco Bay Area	5	25 750
February 2017. Northern CA, San Francisco Bay Area	4 Feb 2017	8 Feb 2017	AR	–	5	5920
March 2018. Central CA coast, the western Sierra Nevada foothills	21 Mar 2018	23 Mar 2018	AR	Narrow cold-frontal rainband	4	1550
February 2019. Statewide	13 Feb 2019	16 Feb 2019	AR	Convective bands in the Sierra Nevada, embedded convection in southern CA	4	5510
April 2020. San Diego County	7 Apr 2020	11 Apr 2020	Cutoff low	Isolated thunderstorms	0	1620
October 2021. Northern CA, San Francisco Bay Area, Sierra Nevada	22 Oct 2021	25 Oct 2021	AR	–	5	60

covered in snow (where shallow landslides are unlikely), we created a mask of sloping terrain greater than 5°, utilizing a 30 m SRTM-derived digital elevation model (DEM) (Farr et al., 2007), and also excluded grid cells with elevations greater than the typical winter snow line in the state (1024 m; see Hatchett et al., 2017). Here we also do not consider the bedrock-dominated deserts east of the Sierra Nevada where our soil moisture storage model for shallow landsliding is not strictly applicable. Although the 5° mask is a low threshold for shallow-landslide-producing hillslopes, we assume a conservative threshold given the relatively large DEM grid size compared to the size of typical shallow landslides. This yields a grid of shallow-landslide-prone terrain throughout the study area. To calculate LPA [km^2] we then interpolated the grid of A^* maxima into the masked hillslope raster and calculated the area of hillslope cells with an A^* maximum equal to or greater than our defined threshold. While here we do not propose that LPA specifically quantifies all areas im-

pacted by landslides, instead we propose this approach offers a reasonable proxy of conditions consistent with observed shallow landsliding that can be used to coordinate potential landslide response.

2.4 Evaluating A^* and LPA for a catalogue of recent landslide-triggering storms

We tested our analytical framework for regional shallow-landslide triggering on a catalogue of nine landslide-inducing storm events that have occurred in California since 2005, including the four calibration events described in Sect. 2.2 (Table 1). While there are notable and well-documented landslide-inducing storms that occurred prior to 2005 in California, the gridded rainfall product we use in our analyses was not available prior to 2005 (Sect. 2.2.1). Thus, we were limited to evaluating only more recent storms. These storms were selected because they were exceptionally large storms with a few well-documented landslide occurrences (essen-

https://doi.org/10.5194/nhess-25-1037-2025

Nat. Hazards Earth Syst. Sci., 25, 1037–1056, 2025

tially null events, e.g., October 2021), had mapped landslides with slightly less constrained timing (e.g., February 2005), or were storms with known reports of extensive landsliding but no available inventories (e.g., December 2005).

For each storm in our catalogue, we also examined the synoptic-scale and mesoscale conditions using a variety of meteorological data. This included analysis of several meteorological variables, such as geopotential height at various levels, integrated water vapor (IWV) and integrated water vapor transport (IVT), and upper-level winds from the ERA5 reanalysis dataset (Hersbach et al., 2020). We used NEXRAD weather radar data archived at the California Nevada River Forecast Office (CNRFC, 2023b) and at the National Centers for Environmental Information (NCEI, 2023) to evaluate spatial patterns of rainfall in storms and to identify areas of short-duration, high-intensity rainfall associated with mesoscale features such as narrow cold-frontal rainbands or thunderstorms, which are represented by high reflectivity values.

We calculated the AR-scale value for each storm using the methodology of Ralph et al. (2019) at all ERA5 grid cells along the Californian coast for a time window spanning 4 d preceding the landslide event of interest; the AR scale requires a minimum 72 h window for calculation. We use the maximum AR scale at landfall in the state as representative of the AR scale of the event. This is common practice in reporting the magnitude of AR events affecting a broad region of interest (e.g., Center for Western Weather and Water Extremes, 2023a) but may differ from the AR-scale value calculated at any individual landslide location. Most events affected multiple parts of the state, or the maximum AR scale at landfall corresponded to the location of one or more of the observed landslides. An exception is the April 2020 San Diego County event. In this event, weak AR conditions were present in the far northern regions of California during the event window but were irrelevant to the event itself, with no AR conditions present south of San Francisco Bay. Thus, it was most appropriate to represent this event as zero – no AR. For the February 2005 Chino Hills event, AR1 conditions were present at a few grid points north of Point Conception, a far distance from the event but still in the broader southern California region. While this event was registered as having AR conditions on the AR scale, it did not feature synoptic features consistent with an AR. Thus, we rank it as AR1 but do not regard it as an AR in the synoptic features column.

3 Data: meteorological characteristics of storms

The nine storms in our catalogue (Table 1) show a range of meteorological characteristics that caused rainfall-induced landslides. The January 2005 and February 2005 storms both impacted southern California, the January 2005 storm caused landslides along the coastal hillslopes and inland canyons of Ventura County (Jibson, 2006; Stock and Bellugi, 2011;

Fig. 1), and the February 2005 storm produced hundreds of landslides in the Chino Hills region east of the city of Los Angeles (Prancevic et al., 2020). Both storms featured atmospheric rivers, with AR-scale values of AR1 and AR3, respectively. They also exhibited embedded convection at the mesoscale, which can produce short bursts of high-intensity rainfall. Both events were also associated with cutoff or closed low-pressure systems. Cutoff lows are mid- to upper-level low-pressure systems that are removed from the mean westerly flow and can result in persistent precipitation in a focused area (Oakley and Redmond, 2014; Barbero et al., 2019), thereby potentially affecting the resultant spatial distribution of landsliding. Localized zones of high-intensity precipitation during or in the vicinity of ARs featured prominently in several storms in our catalogue. For example, the December 2005 storm in northern California featured an extreme atmospheric river (AR4) and produced historic flooding and extensive landsliding across the region (Stock and Bellugi, 2011), including in the San Francisco Bay Area, the Klamath River region, and the Sierra Nevada.

The January 2017 and February 2017 events were part of a series of AR storms during the historically wet season of 2016–2017 in the San Francisco Bay Area that produced over 9000 landslides within the East Bay hills region alone (Corbett and Collins, 2023; Fig. 1). During the January 2017 storm in particular, convective bands of high-intensity precipitation were observed in both the Bay Area and the Sierra Nevada foothills. In the March 2018 event, a stalling narrow cold-frontal rainband occurring immediately after the passage of AR conditions (AR4) produced abundant landslides over a section of the Tuolumne River canyon, west of Yosemite National Park (Collins et al., 2020).

The February 2019 AR storm showed evidence of convective bands in the Sierra Nevada (for reference, approximately 150 km east of the photo in Fig. 1a) and embedded convection in southern California, where historic flooding was observed in Riverside County (Hatchett et al., 2020) and hundreds of landslides occurred (Fig. 3c). The April 2020 storm was a cutoff low-pressure system. As the cutoff low passed over the San Diego region, isolated thunderstorms developed, producing high-intensity rainfall and triggering numerous landslides around the town of Encinitas (Reported California Landslides Database, 2025; Oakley et al., 2020). This storm did not reach classification on the AR scale.

Finally, the October 2021 storm consisted of an AR5 event on 24 October 2021 that pummeled the United States west coast and was the strongest AR to make landfall in northern California in the past 40 years during the month of October (CW3E Event Summary, 2021). This storm led to flooding throughout northern California, in addition to isolated landslides in the northern California Coast Ranges and the northern Sierra Nevada.

4 Results

4.1 Determination of a common A^* threshold for shallow-landslide-triggering conditions

The triggering AWI for landslides from each of the four calibration inventories in our catalogue (January 2005, January 2017, February 2019, and April 2020 storms; Table 1, Fig. 3a–d) varies with the background value of AWI for each location (Fig. 3e). Furthermore, the 10-year recurrence value of AWI (AWI_{10}) appears to serve as a common threshold (i.e., the $1:1$ line) that over 97 % of mapped landslides exceed across the four events. Whereas the January 2017, February 2019, and April 2020 landslide AWI points are closer to this threshold, the January 2005 event plots farther above the $1:1$ line. While this appears to suggest that hillslopes with a higher AWI_{10} may have a comparatively higher triggering threshold, evaluation of more landslide events across a broader climatic gradient is required to test this idea sufficiently. We thus take AWI_{10} as the universal normalization parameter in the calculation of A^* for this analysis (Eq. 1).

Because our definition of A^* utilizes a high storm recurrence interval (i.e., 10 years), A^* values above 1 are, by definition, rare. Yet, we nevertheless find value in looking at the 20-year time series of A^* across each of our landslide calibration sites for which we have consistent rainfall data. For each of the four calibration events, we find that the landslide-inducing storm exhibited the largest peak in A^* across their respective 20-year histories (Fig. 4). At a minimum, this implies setting an A^* threshold of 1 produces no false positives for each site, with the possible exception of the February 2019 Riverside area (Fig. 4c). Here there are two additional above-threshold peaks in the $\sim$ 19-year climatology. The early peak coincides with the January 2005 event, and while we do not have landslide mapping from this event in this region, landslides were indeed reported in surrounding Riverside County from this event (e.g., Los Angeles Times, 2005). Similarly, the second peak in A^* occurred in December 2010 and triggered landslides and debris flows across southern California, including in Riverside County, leading to a request for USD 110 million in federal disaster relief for storm damage (FEMA, 2011). Thus, while we cannot corroborate these two events as producing landslides within the specific boxes due to a lack of detailed landslide inventory information, at the regional scale they may be considered true positives. In the case of the April 2020 storm in the San Diego region, we also show that while the pattern of A^* is somewhat sensitive to the choice of drainage parameter k_d, the timing of the landslide event is captured over several orders of magnitude in k_d (Fig. 5). This suggests that A^* is relatively insensitive to k_d within this region; however more work is required to fully assess how much k_d can influence A^* across landscapes since soil drainage rates are often highly spatially heterogeneous.

When considering false negatives (i.e., distributed shallow landslides associated with A^* values less than 1), assessing their outcome becomes more difficult because we do not have detailed histories of landsliding (or they are absent) at all four sites. However, for the East Bay hills in the San Francisco Bay Area (Figs. 3d and 4d), we do know that the regional distributed landsliding produced by the January 2017 and February 2017 storms (combined number of landslides > 9000) had not previously been observed since the winter of 1997–1998 (Coe and Godt, 2001; Corbett and Collins, 2023). Because these storms occurred so closely in time, it is not possible to determine which of the January or February 2017 storms produced the majority of landslides (Fig. 4b), although both are known to have caused landslides. Notably, both events produced A^* values exceeding 1 within the map area (Fig. 6e and h). Overall, we see that mapped landslides from each of these four calibration storms coincide with peaks in A^* in both space and time, and a common threshold value of $A^* = 1$ based on a comparison to the 10-year climatology can be applied to discriminate the events from storms that occurred in these locations and that did not produce widespread landsliding.

4.2 A^*, LPA, and the impact of atmospheric river strength

All nine storms in our catalogue show at least some patches of above-threshold A^*; however, the magnitude and spatial distribution of A^* are highly variable (Fig. 6). The interquartile ranges of A^* for above-threshold hillslopes mostly occur between 1.0 and 1.1 and do not markedly change with the area of impacted hillslopes (Fig. 7a). Both the January 2005 and the February 2005 storms show larger interquartile ranges of A^* with higher absolute values, and, interestingly, both storms occurred within 2 months of each other in the winter of 2005 and impacted the same regions within southern California (Fig. 6d and g). Both storms had embedded convection and favorable orographic conditions (Table 1), which can lead to locally high rainfall totals (Sect. 4.1). LPA values, which represent the total area of hillslopes experiencing above-threshold A^* for each storm, vary by nearly an order of magnitude and range from approximately 60 km^2 in the case of the October 2021 event to just over $\sim$ 38 000 km^2 in the case of the December 2005 storm that led to severe flooding and landslides across northern California (Figs. 6 and 7).

Given that most storms in our catalogue feature ARs, it is logical to investigate how the magnitude of shallow landsliding, as represented by LPA, compares to the magnitude of the associated AR conditions via the Ralph et al. (2019) AR scale. Our results show that while the largest-LPA events do generally correspond to large-AR events, there is considerable variability between AR magnitude and landslide magnitude (Fig. 7a). For example, the three storms reaching AR5 (January 2017, February 2017, and October 2021) span
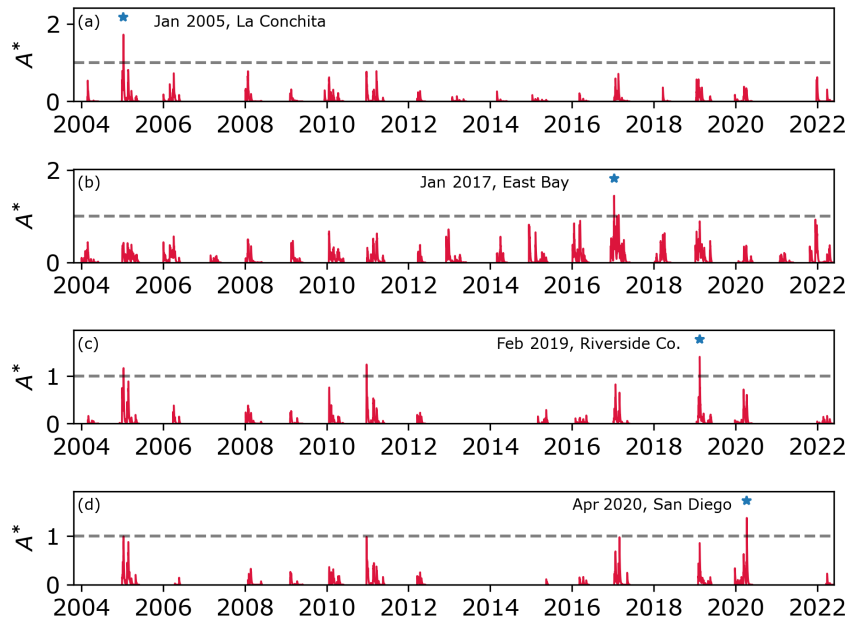
Figure 4. Time series of median A^* within a box surrounding each landslide inventory shown in Fig. 3. The dashed black line corresponds to a threshold value of 1, equivalent to the 10-year recurrence value of the modeled antecedent water index (AWI) (Eq. 2) at each site. Approximate landslide timing (black star) corresponds to the maximum value of A^* across each respective time series. For the case of **(b)**, where landslide observations have been commonplace, no similar instance of extensive landsliding (e.g., Coe and Godt, 2001) has occurred during the modeled interval, indicating no false positives. For the case of **(c)**, the above-threshold peak from December 2010 corresponds to a massive regional storm event that produced numerous landslides and flooding in the region, and the 2005 peak corresponds to the same landslide-inducing storm described in **(a)**, which also produced landslides in Riverside County (see discussion in Sect. 4.1).

the smallest LPA to the second largest (Table 1), indicating limited predictability of landslide hazard from measures of IVT alone. This comports with the findings of Cordeira et al. (2019), who find only a small percentage of reported ARs is associated with reported landslides in the San Francisco Bay Area. One reason for this variability is precisely related to our basing A^* on a model that accounts for antecedent soil moisture conditions. The AR scale does not incorporate any information on antecedent precipitation or soil moisture conditions that may precondition hillslopes and potentially affect subsequent landslide triggering.

Notably, when event LPA is plotted against the month in which the storm occurred, a more systematic relationship becomes apparent (Fig. 7b). Within our event catalogue, the largest landslide responses occur in late December and January and progressively decline throughout the year in an almost-exponential fashion. Although the event catalogue is lacking in spring events relative to winter events, the overall apparent trend indicates that seasonal processes are at play that likely modulate the antecedent hydrologic conditions in landslide-prone hillslopes. This supports our use of a soil water balance (i.e., AWI) anomaly-based metric for identifying landslide-inducing storms; soil moisture generally decreases in the spring months (March–April–May) as storms become less frequent (Fig. 7b), and evapotranspiration increases with longer days and temperatures. Thus, LPA tracks well with

storm frequency metrics, such as the frequency of AR arrivals along the west coast of the United States (Mundhenk et al., 2016), which peaks in December and January and declines similarly to the monthly decline in LPA (Fig. 7b). This is similar to the January peak observed in the monthly frequency of historic landslide days in the San Francisco Bay Area region (Cordiera et al., 2019) and the peak in observed seasonal shallow-landslide activity in the Pacific Northwest (Luna and Korup, 2022), indicating the role of soil moisture storage and groundwater conditions in driving the seasonality of regional shallow-landslide activity (Luna and Korup, 2022). Because A^* and LPA represent local extremes of soil water, this consistent trend across all events suggests that the observed seasonality in LPA persists across the state despite large differences in regional climate.

To test this relationship more explicitly, we examined whether storm LPA correlates with the degree of antecedent A^* values for pixels that ultimately exceeded the landslide threshold during a storm event. Figure 7c reveals a nonlinear relationship where the largest-LPA events in the catalogue tend to have higher antecedent A^* values, and both early-season (e.g., October 2021) and late-season (e.g., April 2020) storms with low-antecedent-A^* conditions exhibit comparatively low LPA values. This relationship is well fit by an exponential function ($R^2 = 0.85$), indicating that, perhaps unsurprisingly, the degree to which the landscape is precondi-
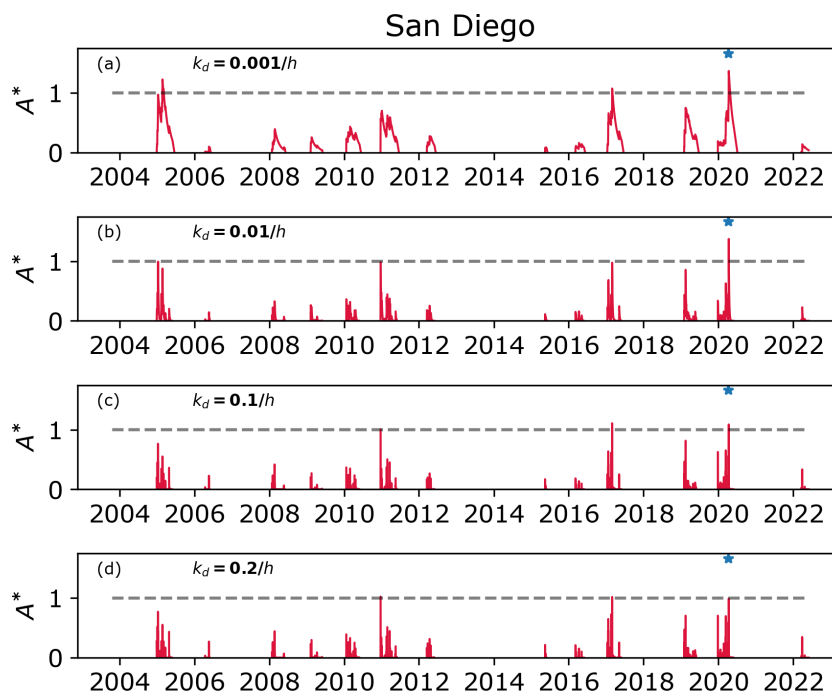
Figure 5. Plots showing the sensitivity of A^* to the drainage coefficient k_d used in the AWI model (Eq. 2) for the San Diego example shown in Fig. 4d. The red lines show the A^* time series for each k_d value ranging from 0.001 **(a)** to $0.2\,\mathrm{h}^{-1}$ **(d)**. Panel **(b)** is the same data as shown in Fig. 4d. The blue star denotes landslide timing in the April 2020 event, and the dashed gray line represents the threshold A^* value of 1 (e.g., Fig. 3). In this example, landslide timing is at or near the threshold value across the range of k_d; however, overall peaks in A^* are broader for slower-draining soils (e.g., **a**) and narrow considerably with increasing drainage rate as the effect of soil storage declines. Thus, peaks in A^* at these drainage rates depend more on instantaneous rainfall intensity and less on multi-day accumulation, which featured prominently in the April 2020 storm (Table 1).

tioned by prior rainfall exerts a strong control on the area impacted by landslide-inducing rainfall. This result may therefore provide a causative link between the apparent relationship between monthly AR arrival frequency and the magnitude of landslide potential area (Fig. 7b), as frequent rainfall events across a region may keep the hydrologic mass balance in an elevated state, making it more prone to exceeding its local threshold should a comparatively strong storm system arrive.

5 Discussion and conclusions

5.1 Effect of low antecedent moisture on large, early-season storm impacts

The October 2021 AR5 storm offers an important example of how low antecedent soil moisture can blunt the impacts of an exceptional storm producing record precipitation in California's highly seasonal climate (Fig. 8). This storm followed a year of drought and came uncharacteristically early for an AR of its magnitude (e.g., Ralph et al., 2019; CW3E Event Summary, 2021). Because of this, soils were close to their residual moisture content. Despite generating a wide swath of highly anomalous 48 h rainfall with R_{48}^* values locally ex-

ceeding values of 2 from the San Francisco Bay Area to the Sierra Nevada (Fig. 8a and b), no reports of major landsliding occurred outside of a few isolated events. Notably, Marc et al. (2019) report R_{48}^* values exceeding 2 as an approximate threshold for what should lead to high-density distributed landsliding. In our calculation of A^*, the initially dry soil conditions at the storm onset that occurred only a few weeks into the rainfall season (beginning 1 October in California) contributed to a diminished distribution of A^* and therefore little predicted landsliding (Fig. 8c). Thus, in Mediterranean climates where dry soils can mitigate the hazardous effects of anomalously high rainfall, consideration of soil storage is an important factor when using normalized thresholds for regional prediction of shallow landslides in soil-mantled hillslopes.

5.2 Dissecting the role of synoptic and mesoscale meteorological processes in landslide hazard

Our study of a wide range of landslide-inducing storms allows for evaluation of the role that storm characteristics might have in the distribution of landslides. We found that while AR presence is often associated with landslide events (e.g., Cordeira et al., 2019), the strength of ARs as measured
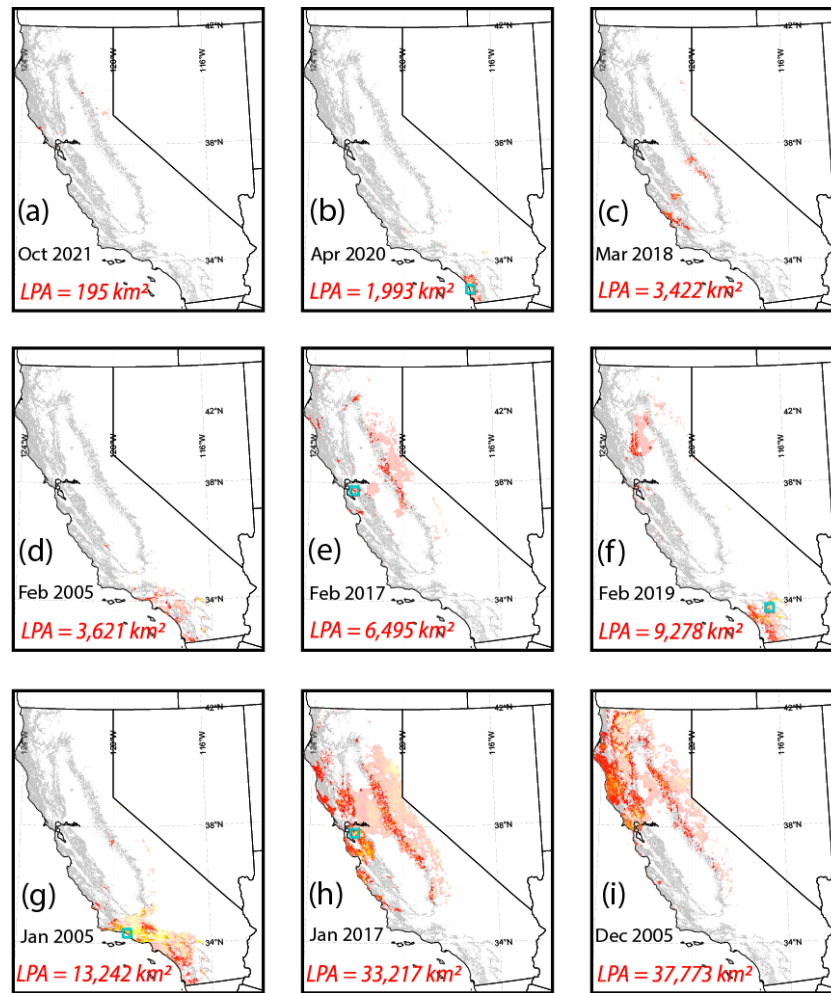
Figure 6. Distributions of A^* and resulting landslide potential area (LPA) for the nine landslide-inducing storms in our catalogue (Table 1). Panels **(a–i)** are ranked in order of increasing LPA: **(a)** October 2021, northern California (CA); **(b)** April 2020, Encinitas; **(c)** March 2018, Central Coast and the Sierra Nevada; **(d)** February 2005, Chino Hills; **(e)** February 2017, northern CA; **(f)** February 2019, Chino Hills and eastern CA; **(g)** January 2005, La Conchita and southern CA; **(h)** January 2017, northern CA; and **(i)** December 2005, northern CA. Hillslopes in our study region are shown in gray, and distributions of A^* are shown as warm colors from $A^* = 1$ (orange) to $A^* \geq 1.75$ (yellow). A^* values outside of hillslopes are semi-transparent, and approximate landslide inventory bounds are shown as teal squares. Topographic data are derived from NASA's SRTM 30 m DEM (NASA, 2013).

by the AR scale did not exert a significant control on the magnitude of landslide-triggering rainfall investigated here (Fig. 7a).

We also find that mesoscale features producing short-duration, high-intensity rainfall may play a more important role in dictating where shallow landslides and associated debris flows occur (Wooten et al., 2008; Coe et al., 2016; Collins et al., 2020). Landslides from the April 2020 storm, one of the events with the smallest LPA values in our catalogue, were triggered by an isolated thunderstorm following a persistent, multi-day period of rainfall associated with a cutoff low-pressure system (Oakley et al., 2020). The mapped landslides spatially correlate with a roughly 10 km wide area of high (> 50 dBZ) radar reflectivity, represent-

ing the isolated effects of the thunderstorm, which also corresponds to a local peak in A^* (Fig. 9a). In a similar example of landslide control by mesoscale processes, extreme rainfall in the March 2018 central California–Sierra Nevada storm event was influenced by a narrow cold-frontal rainband (NCFR) that stalled over the region following the passage of an AR4 atmospheric river (Collins et al., 2020). Here the pattern of landsliding closely matches the radar reflectivity signature of the NCFR passage across the region and the pattern of A^* (Fig. 9b). These two cases in particular highlight how synoptic-scale and mesoscale atmospheric features may work together to produce localized landsliding. In each case, the synoptic feature (cutoff low or atmospheric river) provided long-duration rainfall, which sufficiently primed the
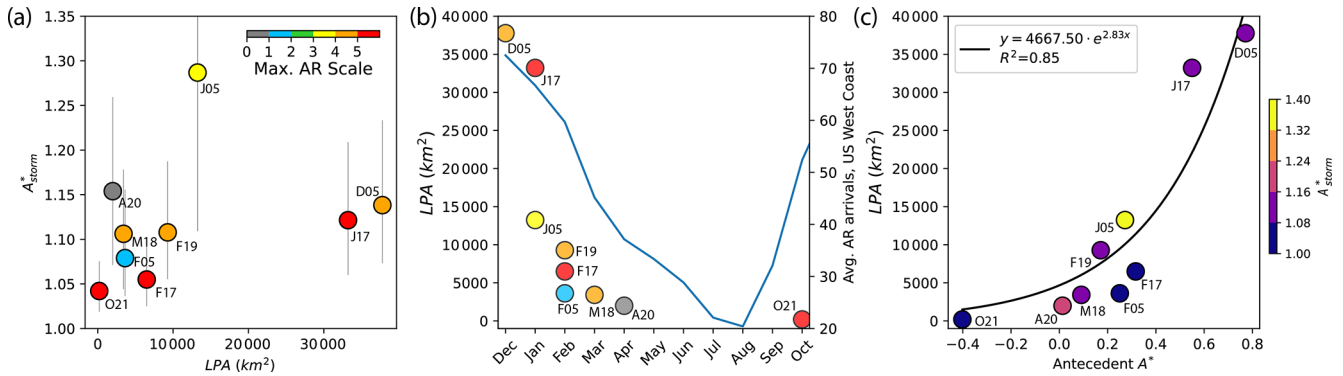
Figure 7. Plots showing the relationship between A^*, landslide potential area (LPA), and the Ralph et al. (2019) atmospheric river (AR) scale. Panel **(a)** shows how the population of above-threshold A^* varies with LPA and the AR scale (color). The dots show the median value of above-threshold A^*, and the vertical lines show the interquartile range. While most events have median values somewhere close to 1, both the January 2005 and the April 2020 events have higher median values above 1.15 and much larger interquartile ranges. This likely reflects the strong orographic and/or convective nature of these two storms in southern California (see discussion). High-AR-scale events exhibit both the highest and the lowest values of LPA in our catalogue. Panel **(b)** shows LPA variation (left axis) with the time of the year. Events in December and January have the highest LPA, with decreasing impacted area (i.e., smaller LPA) later in the rainy season. The right axis shows the average annual AR arrivals along the United States west coast from reanalysis data (Mundhenk et al., 2016). Panel **(c)** shows the relationship between antecedent A^* (the value of A^* preceding a given storm window) for pixels that ultimately exceeded the $A^* = 1$ threshold and resultant LPA. The relationship is well fit by an exponential relationship (black line).
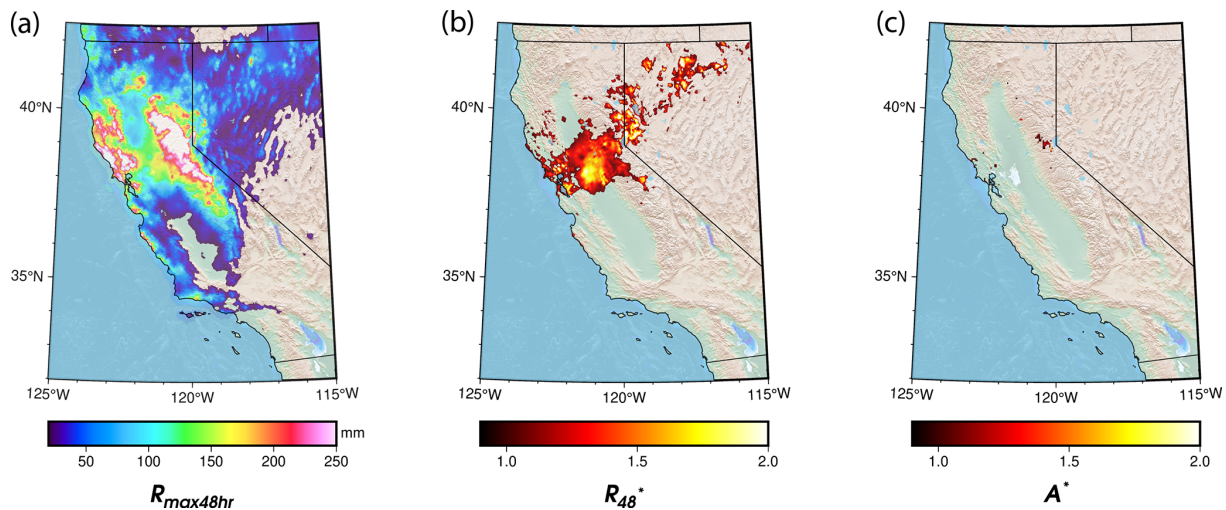
Figure 8. (a) Map showing 48 h maximum precipitation from the 25 October 2021 atmospheric river scale 5 (AR5) that struck northern and central California and produced widespread flooding but few landslides (Table 1). **(b)** R^*_{48} metric of Marc et al. (2019) showing highly anomalous 2 d rainfall totals for the region, calculated by taking the results of panel **(a)** and dividing them by the 10-year recurrence 48 h rainfall estimates from the NOAA Atlas 14 dataset (Perica et al., 2014). **(c)** Map of A^* showing that despite anomalously high rainfall, few impacts from distributed shallow-landslide occurrence may be expected. Shaded relief for all plots is from NASA's SRTM 30 m DEM (NASA, 2013).

soils for failure. This was followed by a high-intensity, short-duration burst of rainfall from a mesoscale feature that acted as a landslide trigger (e.g., Collins et al., 2020; Bogaard and Greco, 2018). The resultant footprint of A^* in these two examples thus directly reflects the passage of mesoscale features.

Conversely, the highest-magnitude LPA event in the dataset, the December 2005 storm in northern California

(LPA of 38 600 km^2), was associated with persistent (multi-hour) moderate-intensity rainfall over broad areas ($\sim$ 200 km scale) (Fig. 9c). This may occur due to the persistence of AR conditions over an area or increased precipitation rates associated with the development of mesoscale frontal waves or secondary cyclones developing near landfalling ARs (e.g., Martin et al., 2019), among other atmospheric processes. The observed rainfall intensities were not as high as the other two
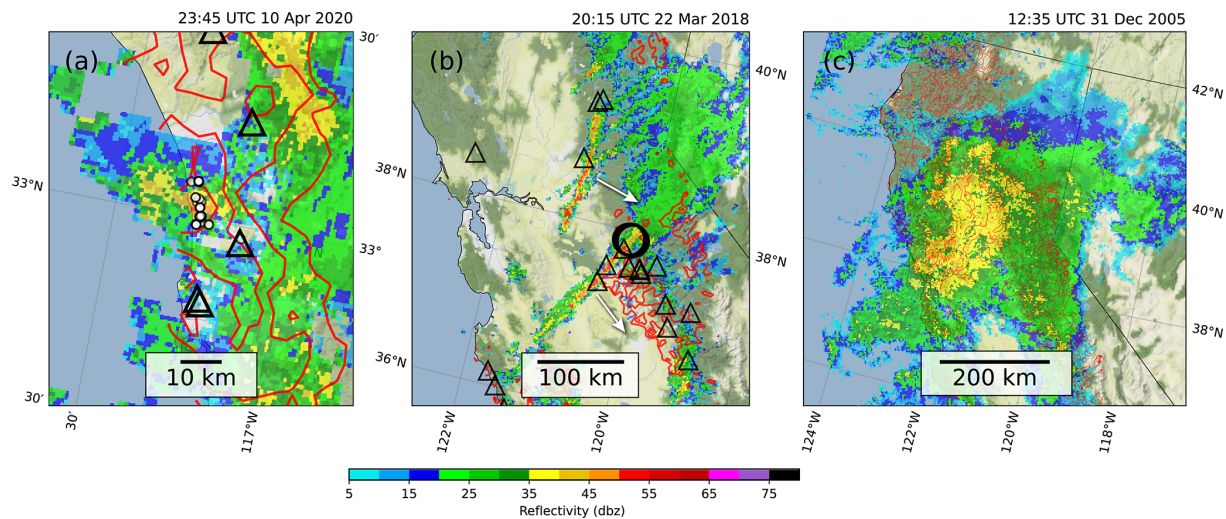
Figure 9. Maps showing examples of a range of spatial scales of precipitation influencing landslide-inducing rainfall distribution in California. Radar reflectivity values are shown as colored pixels, and associated $A^* > 1$ values for each storm are shown as red contours. **(a)** Mesoscale features such as isolated thunderstorms produced very high intensity rainfall and led to localized landslide hotspots in the April 2020 storm in southern California (Table 1; black circles). **(b)** Narrow cold-frontal rainbands (NCFRs), of the order of a few kilometers wide and tens of kilometers long, are another mesoscale feature that can produce high-intensity rainfall, leading to regional zones of landsliding, as was the case along the Sierra Nevada foothills during the March 2018 event (Table 1). The large circles are mapped landslides from Corbett et al. (2020), the triangles are National Weather Service local storm reports of slope failures during the event (Iowa Environmental Mesonet, 2023), and the white arrows show the propagation direction of the NCFRs. **(c)** Broad areas of persistent moderate-intensity precipitation may develop under favorable atmospheric conditions, as in the December 2005 storm in northern California (Table 1), which can lead to widespread distributions of landslide potential area (LPA) when antecedent conditions are sufficiently high over widespread mountainous terrain (Fig. 7c). Map tiles are copyrighted by Stamen Design (2023) under a Creative Commons Attribution (CC BY4.0) license.

events featuring well-defined mesoscale high-intensity rainfall features, but the persistence of moderate-intensity rainfall over an area with very high antecedent A^* (Fig. 7c) resulted in excessively anomalous rainfall at the large regional scale. This region of northern California also has a broader concentration of mountainous terrain than elsewhere in the state (e.g., Fig. 6), which will inherently result in a larger LPA given similar meteorological conditions. Taken together, these results suggest spatial patterns of multi-hour moderate-intensity precipitation and short-duration, high-intensity rainfall can both impact a storm's resulting LPA depending on the antecedent A^* distribution. If hillslope soils are relatively dry over a region, then the post-event pattern of A^* may closely resemble the shape of the meteorological structures that yield the highest-intensity precipitation, which typically occur at a finer spatial scale (e.g., Fig. 9a and b). If the soils preceding a landfalling storm are relatively wet over a broad region, then the pattern of landslide-inducing rainfall may more closely reflect the larger meteorological structures that yield moderate-intensity rainfall (e.g., Fig. 9c). In this way, for many storms the distribution of antecedent A^* may act as an aperture that limits what meteorological structures imprint themselves on the landscape via distributed shallow landsliding.

Due to the role of mesoscale processes in driving landslide-inducing rainfall (Wooten et al., 2008; Minder et al., 2009; Coe et al., 2016; Collins et al., 2020), the quality of the quantitative precipitation estimates (QPEs) used in A^* and the resultant LPA is important. QPEs that incorporate radar observations may better capture smaller-scale convective features that may not be represented by interpolated rain gauge observations such as the CNRFC 6-hourly QPE (CNRFC, 2023a). This is particularly true in landscapes where rain gauges may be heterogeneously distributed. For example, the NCFR passage that drove landsliding in the March 2018 storm was captured well by radar but not particularly well in the rain-gauge-interpolated precipitation dataset along the Sierra Nevada foothills where gauge data are relatively sparse (Fig. 9b). However, QPEs incorporating radar observations may be limited by radar coverage in the complex terrain of the western United States.

5.3 Evaluating A^* performance at the statewide level: an example from the winter 2023 atmospheric river sequence

Concerns also remain as to the degree of predictive success for A^* across a broader range of events and beyond the relatively small regions (approx. 10 to $10\,000\,\mathrm{km}^2$) used for model calibration (e.g., Fig. 3). More systematic and complete landslide inventories are therefore needed at the mega-regional scale (i.e., more than $100\,000\,\mathrm{km}^2$; California is

$424\,000\,\mathrm{km}^2$ in size) to better evaluate how variations in A^* map with changes in both the presence and the absence of landslides and their relative spatial density. Further, if these indices are utilized in decision-making schemes for evaluating risk and regional warning criteria, more work is required to not only examine a broader range of events, particularly large storms that did not trigger landslides, but also evaluate how A^* correlates to landslide triggering across changes in parameters, such as topography, lithology, vegetation, and evapotranspiration. For example, Marc et al. (2019) showed that increasing R^* scales with increasing landslide spatial density, and accounting for lithologic differences further increased correlation. The A^* threshold in this analysis is designed to signify regions of widespread shallow landsliding, but to what extent do increases in A^* correlate with increases in shallow-landslide density, and how sensitive is A^* as a predictor for more isolated landslide events?

Recently, California experienced an extreme-storm sequence of nine back-to-back atmospheric river arrivals from December 2022 to January 2023 (DeFlorio et al., 2024), driving statewide impacts, including flooding, landslides, and debris flows, and significant wind damage that produced an estimated USD 5–7 billion in damages (Moody's RMS, 2023). Throughout the emergency response to the ongoing impacts, the California Geological Survey (CGS) collated and verified reported landslides from state and federal government agencies (i.e., Brien et al., 2023), social media, California Highway Patrol, news reports, and citizen submissions to include in the CGS Reported Landslides Database (2023). The resulting inventory includes over 700 landslide reports from across the state, mostly nearby road networks where observers were located. Although the inventory does not include a full, detailed account of shallow landslides from satellite imagery (e.g., Fig. 3), it covers the entire California study area and thus provides an opportunity to explore how variations in A^* throughout the AR sequence correlate with the location and relative densities of reported landslides. To examine how relative landslide density may correlate with A^* magnitude, we sum the landslide points and spatially average A^* maxima in 15 arcmin ($\sim 20\,\mathrm{km}$) bins (Fig. 10c).

Figure 10 shows snapshots of A^* maxima and reported landslides from the CGS database during two of the most intense storm periods during the 2023 AR sequence: 30 December 2022–3 January 2023 (AR3; Fig. 10a) and 9 January–11 January 2023 (AR3; Fig. 10b). Overall, the footprints of A^* generally cover the zones of high landslide density at the regional scale for both cases. Isolated landslides are not very well resolved by the method; however, some events in the reported landslide database may be related to land use and may not reflect purely natural conditions. Additionally, at this level of mapping it is difficult to evaluate false positives (i.e., zones of above-threshold A^* where reported landslides are absent) because of potential reporting biases. For example, landslides may be under-reported in areas of low road or population density or in instances when certain roads

may have already been closed due to storm damage. Future work with a more robust mapping of natural failures across the entire domain (a time-consuming but essential effort) would help quantify prediction uncertainty and likely provide a more statistically robust relationship between increasing A^* and landslide spatial density. Even so, a gross comparison of reported landslide spatial density with increases in A^* (Fig. 10c) shows a marked rise in landslide spatial density as A^* approaches and exceeds a value of 1, our calibrated threshold based on the local 10-year recurrence of AWI.

Although the climatic normalization process does appear to account for some regional landslide susceptibility differences potentially driven by the geomorphic tuning of the landscape to the regional climate (e.g., Marc et al., 2019), more local site heterogeneity in soil strength and root cohesion likely exert a strong second-order control on landslide triggering during extreme-rainfall events (e.g., McGuire et al., 2016; Rengers et al., 2016; Peruccacci et al., 2017). However, the analysis presented here indicates that A^* is an effective first-order metric for delineating zones of widespread landsliding and can hence serve as a useful guide for the evaluation of regional hazard potential.

5.4 Towards predicting the effects of rainfall-induced landslide hazards

A primary goal of this analysis was to work towards enhancing situational awareness of rainfall-induced shallow-landslide hazard. Global forecast models such as the Global Forecast System (NCEP, 2024) and the European Centre for Medium-Range Weather Forecasts (ECMWF, 2024) provide precipitation forecasts of approximately 2 weeks and can be used as input to provide forecasts of A^* and LPA. Gridded precipitation estimates such as the NOAA Stage IV product (Seo and Breidenbach, 2002; Nelson et al., 2016) could be used to calculate season-to-date A^* in an operational scenario, which itself can provide a glimpse into what potential impacts from an incoming storm may look like (e.g., Fig. 7c). In data-poor regions where calibrated gridded precipitation datasets may not be available, this methodology could be tested using globally available satellite-derived precipitation products. Although the methods developed herein are only applicable for situational awareness of hazardous rainfall at the scale of the precipitation data used, which is typically coarser than the spatial scale of individual hillslopes, one potential advantage is its simplicity of implementation as only rainfall data are needed as model input for A^*. In future work, a more rigorous investigation of model rate constants and additional controls on the water mass balance, such as evapotranspiration, could be investigated. This could be particularly important for Mediterranean climates like California, which are projected to see an increasing number of dry days in a warming climate (Polade et al., 2014).

Nevertheless, our analysis shows that A^* provides a good first-order indication of landslide-inducing rainfall for soil-
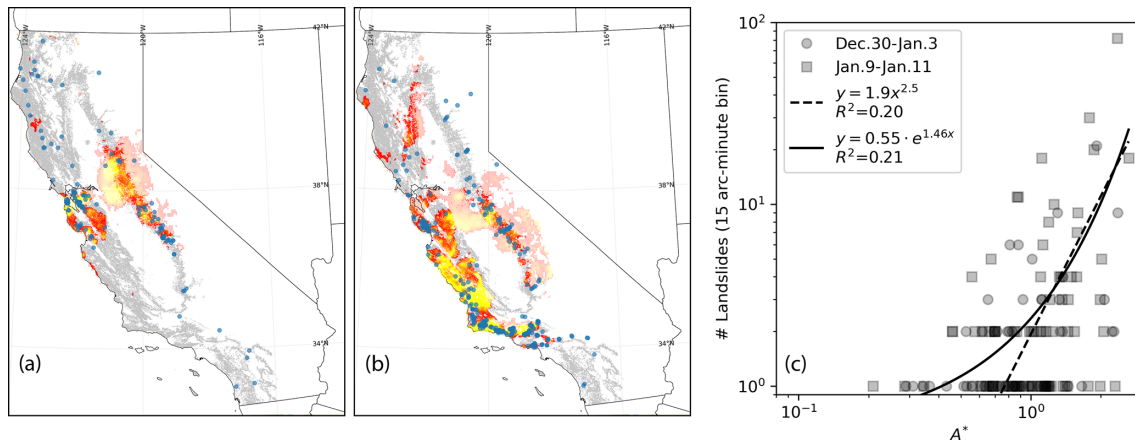
Figure 10. Maps showing distributions of $A*$ maxima and reported landslides during two periods of the December 2022–January 2023 atmospheric river sequence: **(a)** 30 December–3 January, which strongly impacted the San Francisco Bay Area, and **(b)** 9 January–11 January, which strongly impacted the central coast and southern California. The yellow symbols are landslides from each time period from the California Geological Survey Reported Landslides Database. Panel **(c)** shows a plot relating a grid of landslide point density (y axis) to A^* maxima for each respective period in the storm sequence. Although a number of isolated slides show low values of A^*, as A^* approaches 1 landslide density begins to rise rapidly. This highlights the efficacy of the method for identifying zones of widespread landsliding rather than locally isolated events. Shaded relief in **(a)** and **(b)** is from NASA's SRTM 30 m DEM (NASA, 2013).

mantled hillslopes across a range of climatic conditions in California. This simple approach could be used with precipitation forecasts and estimates to provide early warning of landslide hazards and support emergency management decisions ahead of potential events. Additionally, the approach presented here can be used to provide insight into the meteorological and climatic processes that control landslide hazard, conduct intercomparisons of past landslide events, or assess the potential for increased landslide hazard in future storm events for climate model output.

References

Barbero, R., Abatzoglou, J. T., and Fowler, H. J.: Contribution of large-scale midlatitude disturbances to hourly precipitation extremes in the United States, Clim. Dynam., 52, 197–208, https://doi.org/10.1007/s00382-018-4123-5, 2019.

Baum, R. L. and Godt, J. W.: Early warning of rainfall-induced shallow landslides and debris flows in the USA, Landslides, 7, 259–272, https://doi.org/10.1007/s10346-009-0177-0, 2010.

Baum, R. L., Savage, W. Z., and Godt, J. W.: TRIGRS – A Fortran Program for Transient Rainfall Infiltration and Grid-Based Regional Slope-Stability Analysis, Version 2.0, U.S. Geological Survey Open-File Report, 75, https://pubs.usgs.gov/of/2008/1159/ (last access: 27 February 2025), 2008.

Bogaard, T. and Greco, R.: Invited perspectives: Hydrological perspectives on precipitation intensity-duration thresholds for landslide initiation: proposing hydro-meteorological thresholds, Nat. Hazards Earth Syst. Sci., 18, 31–39, https://doi.org/10.5194/nhess-18-31-2018, 2018.

Bogaard, T. A. and Greco, R.: Landslide hydrology: from hydrology to pore pressure, Wiley Interdisciplinary Reviews: Water, 3, 439–459, https://doi.org/10.1002/WAT2.1126, 2016.

Brien, D. L., Collins, B., Corbett, S., and Perkins, J. P.: San Francisco Bay Area Reconnaissance Landslide Inventory, January 2023, US Geological Survey data release, https://doi.org/10.5066/P9NJ3KMG, 2023.

Burrows, K., Marc, O., and Andermann, C.: Retrieval of Monsoon Landslide Timings With Sentinel-1 Reveals the Effects of Earthquakes and Extreme Rainfall, Geophys. Res. Lett., 50, e2023GL104720, https://doi.org/10.1029/2023GL104720, 2023.

Campbell, R. H.: Soil slips, debris flows, and rainstorms in the Santa Monica Mountains and vicinity, southern California, Professional Paper, https://doi.org/10.3133/PP851, 1975.

Cannon, S. H.: Regional rainfall-threshold conditions for abundant debris-flow activity, in: Landslides, Floods, and Marine Effects of the Storm of January 3–5, 1982, in the San Francisco Bay Region, California, edited by: Ellen, S. D., U.S. Geological Survey Professional Paper 1434, 35–42, https://doi.org/10.3133/pp1434, 1988.

Cannon, S. H. and Ellen, S.: Rainfall Conditions for Abundant Debris Avalanches in the San Francisco Bay Region, California, California Geology, 38, 267–272, 1985.

Carlston, C. W.: Drainage density and streamflow, U. S. Geological Survey Professional Paper, 422–C, https://doi.org/10.3133/PP422C, 1963.

Cavagnaro, D. B., McCoy, S. W., Thomas, M. A., Kostelnik, J., and Lindsay, D. N.: The spatial distribution of debris flows in relation to observed rainfall anomalies: Insights from the Dolan Fire, California, E3S Web of Conf., 415, 04003, https://doi.org/10.1051/e3sconf/202341504003, 2023.

CNRFC: QPE (6-Hour Observed Precipitation), California Nevada River Forecast Center [data set], https://www.cnrfc.noaa.gov/arc_search.php?product=netcdfqpe, 2023a.

CNRFC: Radar Archive, California Nevada River Forecast Center, https://www.cnrfc.noaa.gov/radarArchive.php, last access: 2 June 2023b.

Coe, J. A. and Godt, J. W.: Debris flows triggered by the El Nino rainstorm of February 2–3, 1998, Walpert Ridge and vicinity, Alameda County, California, Miscellaneous Field Studies Map, https://doi.org/10.3133/MF2384, 2001.

Coe, J. A., Kean, J. W., Godt, J. W., Baum, R. L., Jones, E. S., Gochis, D. J., and Anderson, G. S.: New insights into debris-flow hazards from an extraordinary event in the Colorado Front Range, GSA Today, 24, 4–10, https://doi.org/10.1130/GSATG214A.1, 2016.

Collins, B. D. and Znidarcic, D.: Stability Analyses of Rainfall Induced Landslides, J. Geotech. Geoenviron., 130, 362–372, https://doi.org/10.1061/(asce)1090-0241(2004)130:4(362), 2004.

Collins, B. D., Oakley, N. S., Perkins, J. P., East, A. E., Corbett, S. C., and Hatchett, B. J.: Linking Mesoscale Meteorology With Extreme Landscape Response: Effects of Narrow Cold Frontal Rainbands (NCFR), J. Geophys. Res.-Earth, 125, e2020JF005675, https://doi.org/10.1029/2020JF005675, 2020.

Corbett, S. C. and Collins, B. D.: Landslides triggered by the 2016–2017 storm season, eastern San Francisco Bay region, California, Scientific Investigations Map, US Geological Survey, https://doi.org/10.3133/sim3503, 2023.

Corbett, S. C. and Perkins, J. P.: Landslides triggered by the January 11th, 2005 storm in the vicinity of La Conchita, Ventura County, CA, USA, US Geological Survey data release [data set], https://doi.org/10.5066/P9K6E6MW, 2024a.

Corbett, S. C. and Perkins, J. P.: Landslides triggered by the February 2019 atmospheric river storm in the vicinity of Bee Canyon, Riverside County, CA, USA, US Geological Survey data release [data set], https://doi.org/10.5066/P92XCRSZ, 2024b.

Corbett, S. C., Oakley, N. S., East, A. E., Collins, B. D., Perkins, J. P., and Hatchett, B. J.: Field, geotechnical, and meteorological data of the 22 March 2018 narrow cold frontal rainband (NCFR) and its effects, Tuolumne River canyon, Sierra Nevada Foothills, California, https://doi.org/10.5066/P9BU8FAQ, 2020.

Cordeira, J. M., Stock, J., Dettinger, M. D., Young, A. M., Kalansky, J. F., and Ralph, F. M.: A 142 year climatology of northern California landslides and atmospheric rivers, B. Am. Meteorol. Soc., 100, 1499–1509, https://doi.org/10.1175/BAMS-D-18-0158.1, 2019.

Crozier, M. J.: Prediction of rainfall-triggered landslides: A test of the antecedent water status model, Earth Surf. Proc. Land., 24, 825–833, https://doi.org/10.1002/(SICI)1096-9837(199908)24:9<825::AID-ESP14>3.0.CO;2-M, 1999.

Crozier, M. J. and Eyles, R. J.: Assessing the probability of rapid mass movement, in: Third Australia-New Zealand conference on Geomechanics, Wellington, New Zealand, 12–16 May 1980, 2-47–2-51, https://search.informit.org/doi/10.3316/informit.649149381088316 (last access: 27 February 2025), 1980.

CW3E Event Summary: 19–26 October 2021, Center For Western Weather and Water Extremes (CW3E), https://cw3e.ucsd.edu/cw3e-event-summary-19-26-october-2021/ (last access: 1 June 2023), 2021.

DeFlorio, M. J., Sengupta, A., Castellano, C. M., Wang, J., Zhang, Z., Gershunov, A., Guirguis, K., Niño, R. L., Clemesha, R. E. S., Pan, M., Xiao, M., Kawzenuk, B., Gibson, P. B., Scheftic, W., Broxton, P. D., Switanek, M. B., Yuan, J., Dettinger, M. D., Hecht, C. W., Cayan, D. R., Cornuelle, B. D., Miller, A. J., Kalansky, J., Monache, L. D., Ralph, F. M., Waliser, D. E., Robertson, A. W., Zeng, X., DeWitt, D. G., Jones, J., and Anderson, M. L.: From California's Extreme Drought to Major Flooding: Evaluating and Synthesizing Experimental Seasonal and Subseasonal

Forecasts of Landfalling Atmospheric Rivers and Extreme Precipitation during Winter 2022/23, B. Am. Meteorol. Soc., 105, E84–E104, https://doi.org/10.1175/BAMS-D-22-0208.1, 2024.

ECMWF: Medium-range forecasts, European Center for Medium-Range Weather Forecasting, https://www.ecmwf.int/en/forecasts/documentation-and-support/medium-range-forecasts, last access: 22 March 2024.

Farr, T. G., Rosen, P. A., Caro, E., Crippen, R., Duren, R., Hensley, S., Kobrick, M., Paller, M., Rodriguez, E., Roth, L., Seal, D., Shaffer, S., Shimada, J., Umland, J., Werner, M., Oskin, M., Burbank, D., and Alsdorf, D. E.: The shuttle radar topography mission, Rev. Geophys., 45, RG2004, https://doi.org/10.1029/2005RG000183, 2007.

FEMA: Winter Storms, Flooding, and Debris and Mud Flows in California, Federal Emergency Management Agency, https://www.fema.gov/es/disaster/1952 (last access: 25 February 2025), 2011.

Froude, M. J. and Petley, D. N.: Global fatal landslide occurrence from 2004 to 2016, Nat. Hazards Earth Syst. Sci., 18, 2161–2181, https://doi.org/10.5194/nhess-18-2161-2018, 2018.

Gabet, E. J., Burbank, D. W., Putkonen, J. K., Pratt-Sitaula, B. A., and Ojha, T.: Rainfall thresholds for landsliding in the Himalayas of Nepal, Geomorphology, 63, 131–143, https://doi.org/10.1016/j.geomorph.2004.03.011, 2004.

Glade, T., Crozier, M., and Smith, P.: Applying Probability Determination to Refine Landslide-triggering Rainfall Thresholds Using an Empirical "Antecedent Daily Rainfall Model", Pure Appl. Geophys., 157, 1059–1079, https://doi.org/10.1007/s000240050017, 2000.

Godt, J. W., Baum, R. L., and Chleborad, A. F.: Rainfall characteristics for shallow landsliding in Seattle, Washington, USA, Earth Surf. Proc. Land., 31, 97–110, https://doi.org/10.1002/ESP.1237, 2006.

Green, W. H. and Ampt, G. A.: Studies on Soil Physics, J. Agr. Sci., 4, 1–24, https://doi.org/10.1017/S0021859600001441, 1911.

Guzzetti, F., Peruccacci, S., Rossi, M., and Stark, C. P.: The rainfall intensity–duration control of shallow landslides and debris flows: an update, Landslides, 5, 3–17, https://doi.org/10.1007/s10346-007-0112-1, 2008.

Guzzetti, F., Gariano, S. L., Peruccacci, S., Brunetti, M. T., Marchesini, I., Rossi, M., and Melillo, M.: Geographical landslide early warning systems, Earth-Sci. Rev., 200, 102973, https://doi.org/10.1016/J.EARSCIREV.2019.102973, 2020.

Hatchett, B. J., Daudert, B., Garner, C. B., Oakley, N. S., Putnam, A. E., and White, A. B.: Winter Snow Level Rise in the Northern Sierra Nevada from 2008 to 2017, Water, 9, 899, https://doi.org/10.3390/w9110899, 2017.

Hatchett, B. J., Cao, Q., Dawson, P. B., Ellis, C. J., Hecht, C. W., Kawzenuk, B., Lancaster, J. T., Osborne, T. C., Wilson, A. M., Anderson, M. L., Dettinger, M. D., Kalansky, J. F., Kaplan, M. L., Lettenmaier, D. P., Oakley, N. S., Ralph, F. M., Reynolds, D. W., White, A. B., Sierks, M., and Sumargo, E.: Observations of an Extreme Atmospheric River Storm With a Diverse Sensor Network, Earth and Space Science, 7, e2020EA001129, https://doi.org/10.1029/2020EA001129, 2020.

Hersbach, H., Bell, B., Berrisford, P., Hirahara, S., Horányi, A., Muñoz-Sabater, J., Nicolas, J., Peubey, C., Radu, R., Schepers, D., Simmons, A., Soci, C., Abdalla, S., Abellan, X., Balsamo, G., Bechtold, P., Biavati, G., Bidlot, J., Bonavita, M., De Chiara, G., Dahlgren, P., Dee, D., Diamantakis, M., Dragani, R., Flemming, J., Forbes, R., Fuentes, M., Geer, A., Haimberger, L., Healy, S., Hogan, R. J., Hólm, E., Janisková, M., Keeley, S., Laloyaux, P., Lopez, P., Lupu, C., Radnoti, G., de Rosnay, P., Rozum, I., Vamborg, F., Villaume, S., and Thépaut, J. N.: The ERA5 global reanalysis, Q. J. Roy. Meteor. Soc., 146, 1999–2049, https://doi.org/10.1002/qj.3803, 2020.

Iowa Environmental Mesonet: IEM Cow (NSW storm based warning verification), Iowa Environmental Mesonet [data set], https://mesonet.agron.iastate.edu/cow/, last access: 2 June 2023.

Iverson, R. M.: Landslide triggering by rain infiltration, Water Resour. Res., 36, 1897–1910, https://doi.org/10.1029/2000WR900090, 2000.

Jenkins, O. P.: Geomorphic Provinces of California as Outlined on the New State Geologic Map: ABSTRACT, AAPG Bull., 22, 1717–1717, https://doi.org/10.1306/3d933068-16b1-11d7-8645000102c1865d, 1938.

Jibson, R. W.: The 2005 La Conchita, California, landslide, Landslides, 3, 73–78, https://doi.org/10.1007/s10346-005-0011-2, 2006.

Keefer, D. K., Wilson, R. C., Mark, R. K., Brabb, E. E., Brown, W. M., Ellen, S. D., Harp, E. L., Wieczorek, G. F., Alger, C. S., and Zatkin, R. S.: Real-Time Landslide Warning During Heavy Rainfall, Science, 238, 921–925, https://doi.org/10.1126/SCIENCE.238.4829.921, 1987.

Kirschbaum, D. and Stanley, T.: Satellite-Based Assessment of Rainfall-Triggered Landslide Hazard for Situational Awareness, Earth's Future, 6, 505–523, https://doi.org/10.1002/2017EF000715, 2018.

Kjekstad, O. and Highland, L.: Economic and social impacts of landslides, Landslides – Disaster Risk Reduction, edited by: Sassa, K. and Canuti, P., Springer, Berlin, Heidelberg, 573–587, https://doi.org/10.1007/978-3-540-69970-5_30, 2009.

Kong, V. W. W., Kwan, J. S. H., and Pun, W. K.: Hong Kong's landslip warning system – 40 years of progress, Landslides, 17, 1453–1463, https://doi.org/10.1007/s10346-020-01379-6, 2020.

Lamjiri, M. A., Ralph, F. M., and Dettinger, M. D.: Recent Changes in United States Extreme 3-Day Precipitation Using the R-CAT Scale, J. Hydrometeorol., 21, 1207–1221, https://doi.org/10.1175/JHM-D-19-0171.1, 2020.

Larsen, M. C. and Simon, A.: A rainfall intensity-duration threshold for landslides in a humid- tropical environment, Puerto Rico, Geogr. Ann. A, 75A, 13–23, https://doi.org/10.1080/04353676.1993.11880379, 1993.

Los Angeles Times: Mudslide Buries Houses, Kills 3 in Ventura County, https://www.latimes.com/archives/la-xpm-2005-jan-11-me-rain11-story.html (last access: 26 February 2025), 2005.

Lu, N., Kaya, B. S., and Godt, J. W.: Direction of unsaturated flow in a homogeneous and isotropic hillslope, Water Resour. Res., 7, W02519, https://doi.org/10.1029/2010WR010003, 2011.

Luna, L. V. and Korup, O.: Seasonal Landslide Activity Lags Annual Precipitation Pattern in the Pacific Northwest, Geophys. Res. Lett., 49, e2022GL098506, https://doi.org/10.1029/2022GL098506, 2022.

Marc, O., Meunier, P., and Hovius, N.: Prediction of the area affected by earthquake-induced landsliding based on seismological parameters, Nat. Hazards Earth Syst. Sci., 17, 1159–1175, https://doi.org/10.5194/nhess-17-1159-2017, 2017.

Marc, O., Gosset, M., Saito, H., Uchida, T., and Malet, J. P.: Spatial Patterns of Storm-Induced Landslides and Their Relation to Rainfall Anomaly Maps, Geophys. Res. Lett., 46, 11167–11177, https://doi.org/10.1029/2019GL083173, 2019.

Martin, A. C., Ralph, F. M., Wilson, A., DeHaan, L., and Kawzenuk, B.: Rapid Cyclogenesis from a Mesoscale Frontal Wave on an Atmospheric River: Impacts on Forecast Skill and Predictability during Atmospheric River Landfall, J. Hydrometeorol., 20, 1779–1794, https://doi.org/10.1175/JHM-D-18-0239.1, 2019.

McGuire, L. A., Rengers, F. K., Kean, J. W., Coe, J. A., Mirus, B. B., Baum, R. L., and Godt, J. W.: Elucidating the role of vegetation in the initiation of rainfall-induced shallow landslides: Insights from an extreme rainfall event in the Colorado Front Range, Geophys. Res. Lett., 43, 9084–9092, https://doi.org/10.1002/2016GL070741, 2016.

Minder, J. R., Roe, G. H., and Montgomery, D. R.: Spatial patterns of rainfall and shallow landslide susceptibility, Water Resour. Res., 45, W04419, https://doi.org/10.1029/2008WR007027, 2009.

Mirus, B. B., Bogaard, T. A., Greco, R., and Stähli, M.: Invited Perspectives: Integrating hydrologic information into the next generation of landslide early warning systems, EGUsphere [preprint], https://doi.org/10.5194/egusphere-2024-1219, 2024.

Montgomery, D. R. and Dietrich, W. E.: A physically based model for the topographic control on shallow landsliding, Water Resour. Res., 30, 1153–1171, https://doi.org/10.1029/93WR02979, 1994.

Moody's RMS: Moody's RMS estimates US$5–7 billion in total U. S. economic losses from California Flooding. Moody's RMS, https://www.rms.com/newsroom/press-releases/press-detail/2023-01-25/moodys-rms-estimates-us5-7-billion-in-total-us-economic-losses-from-california-flooding (last access: 8 February 2024), 2023.

Mundhenk, B. D., Barnes, E. A., and Maloney, E. D.: All-Season Climatology and Variability of Atmospheric River Frequencies over the North Pacific, J. Climate, 29, 4885–4903, https://doi.org/10.1175/JCLI-D-15-0655.1, 2016.

NASA: Shuttle Radar Topography Mission (SRTM) Global, SRTM – Shuttle Radar Topography Mission, OpenTopography [data set], https://doi.org/10.5069/G9445JDF, 2013.

NCEP: NOAA/NCEP Global Forecast System (GFS) Atmospheric Model, NOAA National Centers for Environmental Prediction, https://www.ncei.noaa.gov/products/weather-climate-models/global-forecast, (last access: 22 March 2024), 2024.

Nelson, B. R., Prat, O. P., Seo, D. J., and Habib, E.: Assessment and implications of NCEP stage IV quantitative precipitation estimates for product intercomparisons, Weather Forecast., 31, 371–394, https://doi.org/10.1175/WAF-D-14-00112.1, 2016.

Nemani, R., White, M., Thornton, P., Nishida, K., Reddy, S., Jenkins, J., and Running, S.: Recent trends in hydrologic balance have enhanced the terrestrial carbon sink in the United States, Geophys. Res. Lett., 29, 106-1–106-4, https://doi.org/10.1029/2002GL014867, 2002.

Oakley, N. S. and Redmond, K. T.: A Climatology of 500-hPa Closed Lows in the Northeastern Pacific Ocean, 1948–2011, J. Appl. Meteorol. Clim., 53, 1578–1592, https://doi.org/10.1175/JAMC-D-13-0223.1, 2014.

Oakley, N. S., Lancaster, J. T., Hatchett, B. J., Stock, J., Ralph, F. M., Roj, S., and Lukashov, S.: A 22 year climatology of cool season hourly precipitation thresholds conducive to shallow landslides in California, Earth Interact., 22, 1–35, https://doi.org/10.1175/EI-D-17-0029.1, 2018.

Oakley, N. S., de Orla-Barile, M., Hatchett, B., Burgess, W. P., and Ralph, F. M.: Characteristics and Impacts of the April 4–11 2020 Cutoff Low Storm in California, Center For Western Weather and Water Extremes (CW3E), https://cw3e.ucsd.edu/characteristics-and-impacts-of-the-april-4-11-2020-cutoff-low-storm-in-california/ (last access: 2 June 2023), 2020.

Okada, K., Makihara, Y., Shimpo, A., Nagata, K., Kunitsugu, M., and Saito, H.: Soil Water Index, Tenki, 47, 36–41, 2001.

Osanai, N., Shimizu, T., Kuramoto, K., Kojima, S., and Noro, T.: Japanese early-warning for debris flows and slope failures using rainfall indices with Radial Basis Function Network, Landslides, 7, 325–338, https://doi.org/10.1007/s10346-010-0229-5, 2010.

Pelletier, J. D., Broxton, P. D., Hazenberg, P., Zeng, X., Troch, P. A., Niu, G. Y., Williams, Z., Brunke, M. A., and Gochis, D.: A gridded global data set of soil, intact regolith, and sedimentary deposit thicknesses for regional and global land surface modeling, J. Adv. Model. Earth Sy., 8, 41–65, https://doi.org/10.1002/2015MS000526, 2016.

Perica, S., Dietz, S., Heim, S., Hiner, L., Maitaria, K., Martin, D., Pavlovic, S., Roy, I., Trypaluk, C., Unruh, D., Yan, F., Yekta, M., Zhao, T., Bonnin, G., Brewer, D., Chen, L.-C., Parzybok, T., and Yarchoan, J.: Precipitation-Frequency Atlas of the United States, Version 2.3, California, United States, National Weather Service [data set], https://repository.library.noaa.gov/view/noaa/22614 (last access: 26 February 2025), 2014.

Peruccacci, S., Brunetti, M. T., Gariano, S. L., Melillo, M., Rossi, M., and Guzzetti, F.: Rainfall thresholds for possible landslide occurrence in Italy, Geomorphology, 290, 39–57, https://doi.org/10.1016/J.GEOMORPH.2017.03.031, 2017.

Petley, D.: Global patterns of loss of life from landslides, Geology, 40, 927–930, https://doi.org/10.1130/G33217.1, 2012.

Polade, S. D., Pierce, D. W., Cayan, D. R., Gershunov, A., and Dettinger, M. D.: The key role of dry days in changing regional climate and precipitation regimes, Sci. Rep.-UK, 4, 4364, https://doi.org/10.1038/srep04364, 2014.

Prancevic, J. P., Lamb, M. P., McArdell, B. W., Rickli, C., and Kirchner, J. W.: Decreasing Landslide Erosion on Steeper Slopes in Soil-Mantled Landscapes, Geophys. Res. Lett., 47, e2020GL087505, https://doi.org/10.1029/2020GL087505, 2020.

PRISM: 30-Year Normals, PRISM Climate Group, Oregon State University [data set], https://prism.oregonstate.edu/ (last access: 6 June 2023), 2014.

Ralph, F., Rutz, J. J., Cordeira, J. M., Dettinger, M., Anderson, M., Reynolds, D., Schick, L. J., and Smallcomb, C.: A Scale to Characterize the Strength and Impacts of Atmospheric Rivers, B. Am. Meteorol. Soc., 100, 269–289, https://doi.org/10.1175/BAMS-D-18-0023.1, 2019.

Ralph, F. M. and Dettinger, M. D.: Historical and National Perspectives on Extreme West Coast Precipitation Associated with Atmospheric Rivers during December 2010, B. Am. Meteorol. Soc., 93, 783–790, https://doi.org/10.1175/BAMS-D-11-00188.1, 2012.

Reid, M. E.: A pore-pressure diffusion model for estimating landslide-inducing rainfall, J. Geol., 102, 709–717, https://doi.org/10.1086/629714, 1994.

Rengers, F. K., McGuire, L. A., Coe, J. A., Kean, J. W., Baum, R. L., Staley, D. M., and Godt, J. W.: The influence of vegetation on debris-flow initiation during extreme rainfall in the northern Colorado Front Range, Geology, 44, 823–826, https://doi.org/10.1130/G38096.1, 2016.

Reported California Landslides Database: https://www.conservation.ca.gov/cgs/landslides, last access: 25 February 2025.

Richards, L. A.: Capillary conduction of liquids through porous mediums, J. Appl. Phys., 1, 318–333, https://doi.org/10.1063/1.1745010, 1931.

Richardson, L. F.: Weather Prediction by Numerical Process, Cambridge University Press, 260 pp., ISBN 0521680441, ISBN 9780521680448, 1922.

Richardson, P. W., Perron, J. T., and Schurr, N. D.: Influences of climate and life on hillslope sediment transport, Geology, 47, 423–426, https://doi.org/10.1130/G45305.1, 2019.

Saito, H. and Matsuyama, H.: Catastrophic Landslide Disasters Triggered by Record-Breaking Rainfall in Japan: Their Accurate Detection with Normalized Soil Water Index in the Kii Peninsula for the Year 2011, SOLA, 8, 81–84, https://doi.org/10.2151/SOLA.2012-021, 2012.

Saito, H., Nakayama, D., and Matsuyama, H.: Two Types of Rainfall Conditions Associated with Shallow Landslide Initiation in Japan as Revealed by Normalized Soil Water Index, SOLA, 6, 57–60, https://doi.org/10.2151/SOLA.2010-015, 2010.

Schmidt, K. M., Roering, J. J., Stock, J. D., Dietrich, W. E., Montgomery, D. R., and Schaub, T.: The variability of root cohesion as an influence on shallow landslide susceptibility in the Oregon Coast Range, Can. Geotech. J., 38, 995–1024, https://doi.org/10.1139/cgj-38-5-995, 2001.

Schuster, R. L. and Fleming, R. W.: Economic Losses and Fatalities Due to Landslides, Environ. Eng. Geosci., xxiii, 11–28, https://doi.org/10.2113/GSEEGEOSCI.XXIII.1.11, 1986.

Seo, D. J. and Breidenbach, J. P.: Real-time correction of spatially nonuniform bias in radar rainfall data using rain gauge measurements, J. Hydrometeorol., 3, 93–111, https://doi.org/10.1175/1525-7541(2002)003<0093:RTCOSN>2.0.CO;2, 2002.

Stock, J. D. and Bellugi, D.: An empirical method to forecast the effect of storm intensity on shallow landslide abundance, Italian Journal of Engineering Geology and Environment, Special Issue: V Conference Debris Flow, 1013–1022, https://doi.org/10.4408/IJEGE.2011-03.B-110, 2011.

Tanyaş, H. and Lombardo, L.: Variation in landslide-affected area under the control of ground motion and topography, Eng. Geol., 260, 105229, https://doi.org/10.1016/j.enggeo.2019.105229, 2019.

Tao, S., Guo, Q., Li, C., Wang, Z., and Fang, J.: Global patterns and determinants of forest canopy height, Ecology, 97, 3265–3270, https://doi.org/10.1002/ECY.1580, 2016.

Thomas, M. A., Mirus, B. B., and Collins, B. D.: Identifying Physics-Based Thresholds for Rainfall-Induced Landsliding, Geophys. Res. Lett., 45, 9651–9661, https://doi.org/10.1029/2018GL079662, 2018.

Tian, D., Uieda, L., Leong, W. J., Fröhlich, Y., Schlitzer, W., Grund, M., Jones, M., Toney, L., Yao, J., Tong, J.-H., Magen, Y., Materna, K., Belem, A., Newton, T., Anant, A., Ziebarth, M., Quinn, J., and Wessel, P.: PyGMT: A Python interface for the Generic Mapping Tools, Zenodo [code], https://doi.org/10.5281/zenodo.14868324, 2025.

Tucker, G. E. and Slingerland, R.: Drainage basin responses to climate change, Water Resour. Res., 33, 2031–2047, https://doi.org/10.1029/97WR00409, 1997.

van Genuchten, M. Th.: A Closed-form Equation for Predicting the Hydraulic Conductivity of Unsaturated Soils, Soil Sci. Soc. Am. J., 44, 892–898, https://doi.org/10.2136/sssaj1980.03615995004400050002x, 1980.

Wilson, R. C.: Normalizing rainfall/debris-flow thresholds along the U. S. Pacific coast for long-term variations in precipitation climate, in: Proceedings of the 1997 1st International Conference on Debris-Flow Hazards Mitigation: Mechanics, Prediction, and Assessment, 7–9 August 1997, San Francisco, CA, USA, 32–43, https://pubs.er.usgs.gov/publication/70020201 (last access: 27 February 2025), 1997.

Wilson, R. C. and Jayko, A. S.: Preliminary maps showing rainfall thresholds for debris-flow activity, San Francisco Bay region, California, Open-File Report, US Dept. of the Interior, US Geological Survey, https://doi.org/10.3133/ofr97745F, 1997.

Wilson, R. C. and Wieczorek, G. F.: Rainfall thresholds for the initiation of debris flows at La Honda, California, Environ. Eng. Geosci., 1, 11–27, 1995.

Wooten, R. M., Gillon, K. A., Witt, A. C., Latham, R. S., Douglas, T. J., Bauer, J. B., Fuemmeler, S. J., and Lee, L. G.: Geologic, geomorphic, and meteorological aspects of debris flows triggered by Hurricanes Frances and Ivan during September 2004 in the Southern Appalachian Mountains of Macon County, North Carolina (southeastern USA), Landslides, 5, 31–44, https://doi.org/10.1007/s10346-007-0109-9, 2008.